Insights into Deep Mantle Thermochemical Contributions to African Magmatism from Converted Seismic Phases

A. Boyce[1], S. Cottaar[1]

[1]University of Cambridge, Department of Earth Science, Bullard Laboratories, Madingley Road, Cambridge, CB3 0EZ, UK.

Key Points:

- We investigate mantle transition zone and mid mantle discontinuity structure below Africa using P to s receiver functions
- A thin transition zone underlies East African Cenozoic magmatism implying influence of processes at mantle transition zone depths or below
- A thermochemically distinct upwelling underlies Kenya while a purely thermal upwelling underlies Ethiopia

Corresponding author: Alistair Boyce, `ab2568@cam.ac.uk`

Abstract

The contribution of mantle upwellings of varying spatial extent to Cenozoic magmatism across Africa is debated because geochemical and seismological tools used to interrogate them are primarily sensitive to either composition or temperature. Thermochemical conditions control the depth at which mantle materials undergo phase changes, which cause seismic discontinuities. Mapping seismic discontinuities across the mantle transition zone (MTZ) and below provides insight into the variable thermochemical nature of upwellings. We present observations of seismic discontinuities beneath Africa obtained from a compilation of P-to-s receiver functions (using Pds, PPds, and PKPds phases), recorded at seismograph networks across Africa between 1990–2019. We exploit a recent high-resolution African continental P-wavespeed model to migrate our receiver functions to depth in a common conversion point stack. Cenozoic magmatism along the East African Rift is largely underlain by a thin MTZ implying a contribution to rift magmatism from sources at or below MTZ depths. The Ethiopian rift is underlain by a depressed d410 and uplifted d660 indicating a moderate positive thermal anomaly at MTZ depths ($\sim$100–150 K). The southern East African Rift displays a greater d410 depression and a regional d660 depression, suggesting a stronger thermochemical anomaly at MTZ depths. Here, seismic conversions at $\sim$1025 km depth are collocated with slow wavespeeds within the African Superplume, corroborating evidence for a compositional anomaly. We suggest that the contribution of a purely thermal plume directly below Ethiopia augments conditions for mantle melting and rifting. Distinct upwellings may also affect the MTZ below Cenozoic magmatism in Cameroon and Madagascar.

Plain Language Summary

The African plate has experienced widespread Cenozoic hotspot and rift-related activity during the development of the East African Rift, the Cameroon Volcanic Line and other magmatic provinces e.g., central Madagascar. Warmed by the Earth's core, hot mantle rock rises slowly over millions of years within mantle plumes, and melts upon reaching the near-surface. Mantle plumes may therefore be partly responsible for the formation of volcanoes and crustal magmatism across Africa. However, the number, size and physical properties of African mantle plumes are debated because geochemical and seismic imaging techniques often used to investigate them are typically sensitive to temperature or mineral chemistry. Instead, we measure the depth at which seismic waves undergo conversions from compressional-to-transverse that reflect where mantle minerals undergo changes in their crystal structure. This informs us of variations in both temperature and mineral chemistry in the mantle because both factors affect the precise crystal rearrangement depths. Mantle plumes rooted below 1000 km depth may exist below East Africa and perhaps also, Cameroon and Madagascar. Specifically, warm mantle rising below Kenya and Madagascar may transport material from chemically distinct regions on the core-mantle boundary. Plumes elsewhere are likely purely thermal in nature, not sampling chemically distinct deep mantle regions.

AGU "index terms": Africa – Receiver Functions – Mantle Transition Zone – Hotspots, large igneous provinces, and flood basalt magmatism – Earth's interior: composition and state

1 Introduction

1.1 Background

The African plate hosts numerous loci of Cenozoic magmatism (Figure 1). In East Africa, uplifted plateaus (e.g., Lithgow-Bertelloni & Silver, 1998; Pik et al., 2003; Pik et al., 2008) and emplacement of the Ethiopian flood basalt province at $\sim$30 Ma (e.g., Chorowicz, 2005; Rooney, 2017) are associated with the rift-related igneous activity continuing to the present day. Here, magmatism and uplift has previously been explained by one or more mantle plumes (Ebinger & Sleep, 1998; George et al., 1998; Rogers et al., 2000; Furman, Bryce, et al., 2006; Pik et al., 2006), but whether they originate in the lower mantle, and the extent to which they are purely thermal or thermochemical in nature is debated (e.g., Nelson et al., 2012; Rooney, 2017).

In west Africa, the Cameroon Volcanic Line (CVL) is a linear volcanic chain straddling the continent-ocean boundary. Initially explained in the context of traditional plume-plate interactions, leading to inclusion with global deep-mantle hotspot catalogs (Courtillot et al., 2003; French & Romanowicz, 2015), the CVL's lack of age progression has given rise to numerous subsequent alternative formation hypotheses. Such hypotheses include small-scale convection (e.g., King & Ritsema, 2000; Reusch et al., 2011), shear zone reactivation (e.g., Fairhead, 1988), lithospheric delamination (e.g., Milelli et al., 2012; De Plaen et al., 2014), and inflow of material from Ethiopia/Afar (e.g., Ebinger & Sleep, 1998). Whether CVL magmatism requires any contribution from the lower mantle is therefore uncertain.

Elsewhere, Madagascan Cenozoic magmatism has been postulated to arise from decompression melting associated with regional uplift, lithospheric thinning and intracontinental rifting with limited contributions from subplate thermal anomalies (e.g., Melluso et al., 2016; Cucciniello et al., 2017). However influx of plume material below the northern magmatic province specifically, has previously been suggested (Ebinger & Sleep, 1998). Below recent magmatism in central Madagascar, the presence of thermal anomalies that may extend below the shallow mantle ($>$200 km) is unresolved (e.g., Cucciniello et al., 2017; Pratt et al., 2017) because seismic station coverage has only recently expanded (e.g., Wysession et al., 2011; Tilmann et al., 2012), meaning body wave constraints capable of resolving this issue are presently lacking.

Africa's deep mantle structure is characterized by the African Superplume (e.g., Ni et al., 2002; Simmons et al., 2007). This broad, $>$500 km wide inclined upwelling appears to rise from the Large Low Velocity Province (LLVP) on the core-mantle boundary below southern Africa, reaching upper mantle depths somewhere below the East African Rift System (e.g., Ritsema et al., 2011; Cottaar & Lekić, 2016). This feature has been imaged frequently by seismic tomography (e.g., Ritsema et al., 1999, 2011; Li et al., 2008), however more recent high resolution studies indicate the presence of multiple upwellings with a variety of depth extents (e.g., Chang & Van der Lee, 2011; Civiero et al., 2015; Boyce et al., 2021). Tomographic images often suffer along-raypath smearing, underestimation of anomaly amplitudes, and are typically inadequate to allow discrimination between the competing effects of thermal and compositional variation on seismic wavespeed in the sublithospheric mantle. Consequently tomographic models have not been able to robustly constrain the thermochemical contribution to magmatism from mid-to-lower mantle depths (e.g., Reusch et al., 2010; Adams et al., 2015; Pratt et al., 2017; Boyce et al., 2021; Emry et al., 2019).

Petrological evidence for high $^{3}He/^{4}He$ ratios in Ethiopia specifically (up to R/Ra$\approx$20), presents clear evidence for a deep mantle contribution to East African Cenozoic magmatism (e.g., Marty et al., 1996; Pik et al., 2006). More recent studies have presented elevated helium isotopic ratios observed in the southern East African Rift as evidence for a common lower mantle source for all East African magmatism

(Hilton et al., 2011; Halldórsson et al., 2014). However, the relative proximity of proposed mantle upwellings (e.g., George et al., 1998; Rogers et al., 2000), limited depth resolution, variable sampling strategies and lithospheric contamination (e.g., Furman, Bryce, et al., 2006; Barry et al., 2013) limit the capability of such studies to conclusively decipher between competing models of African mantle upwellings (Rooney, 2017). A high resolution, continent-wide investigation capable of constraining thermochemical contributions to African magmatism from below the upper mantle is therefore required.

Thermochemical conditions control the depth at which mantle materials undergo phases changes (e.g., Xu et al., 2008), which cause seismic impedance contrasts of varying amplitude (e.g., Bina & Helffrich, 1994; Helffrich & Wood, 1996; Buchen et al., 2018). Compositional variations may also give rise to further phase transitions not predicted within a well mixed, pyrolitic composition (e.g., Murakami et al., 2005; Nomura et al., 2010). Upon encountering impedance contrasts, seismic energy can convert from P-to-s and vice versa. Processing of seismic waveforms to extract receiver functions (RFs) highlights these conversions in the seismogram, and when stacked appropriately can elucidate the depth at which phase transitions occur. RFs, processed to target mantle transition zone (MTZ) depths and below, can therefore be used to probe the thermal and compositional impact of heterogeneous upwellings below Africa.

Regional studies of the African MTZ are legion (e.g., Owens et al., 2000; Gao et al., 2002; Benoit et al., 2006; Reusch et al., 2011; Lemnifi et al., 2019) and have been revisited periodically as new networks have been deployed. Continent-wide studies are scarce and primarily focus on single station stacks from few permanent observatory sites (e.g., Julià & Nyblade, 2013). RF studies often show conflicting results, in part due to variable and/or inadequate time-to-depth corrections applied based on 1D radial Earth models or relative arrival-time tomographic models. Here we present a continent-wide compilation of P-to-s receiver functions (obtained from P, PP and PKP phases) recorded at 947 publicly available African seismograph stations from 1990–2019 (Figure 1). We capitalize on the recent high-resolution absolute arrival-time P-wavespeed tomographic model for Africa of Boyce et al. (2021) to convert our RFs from time-to-depth, and compare against results from four other S-wavespeed models. This consistent continent-wide data processing approach enables us to compare MTZ discontinuity topography beneath regions of mantle upwellings across Africa. We consider whether RF data can provide evidence in support of multiple mantle plumes below the East African Rift System, and specifically if these upwellings manifest as two thermochemically distinct regions at MTZ depths and below. We also interrogate our continental RF data set for insights into the nature of mantle upwellings below magmatism in Madagascar and Cameroon.

1.2 Mantle Discontinuities, Causes and Topography

Important to investigating the variable impact of upwellings on mantle discontinuity structure below the African continent is an understanding of seismically observable diagnostics of mantle thermochemical heterogeneity sampled by RF techniques. While comprehensive reviews can be found in Bina and Helffrich (1994); Helffrich (2000); Deuss et al. (2013) and Kaneshima (2016), here we briefly summarize the characteristics and causal mechanisms of mantle discontinuities in the depth range $\sim$350–1200 km. The dominant mineralogical component of mantle rock is olivine, making up 40–60%. The most abrupt phase changes in the olivine system are expressed as the upper and lower discontinuities of the mantle transition zone at $\sim$410 km depth, where olivine transitions to wadsleyite, and at $\sim$660 km where ringwoodite transitions to bridgmanite and ferropericlase. We refer to these transition depths as d410 and d660 respectively and their converted phases by phase names bounding the discontinuity depth from which they are converted (e.g., P410s, PP660s). The transition from

wadsleyite to ringwoodite at ∼520 km is thought to be more gradational and is only intermittently observed (Deuss & Woodhouse, 2001; Julià & Nyblade, 2013).

The olivine to wadsleyite transition at ∼410 km displays a positive Clapeyron slope such that the transition occurs at greater depth in regions of higher temperature, and promotes mass transfer (e.g., Davies, 1995). Clapeyron slope estimates center on ∼+3.0 MPa/K (e.g., Bina & Helffrich, 1994), but literature values can vary (∼+1.5 – +4.0 MPa/K: Akaogi et al., 1989; Katsura et al., 2004). In MTZ RF analyses, the P410s conversion typically manifests as a single peak arrival, but variations in transition sharpness/impedance contrast (reflected in signal peak broadness) can be affected by composition (including water content) and temperature (e.g., Helffrich & Wood, 1996; Buchen et al., 2018).

The lower MTZ phase transition is typically dominated by the transition from ringwoodite to bridgmanite and ferropericlase at ∼660 km. It displays a negative Clapeyron slope of –2.5 MPa/K (e.g., Ye et al., 2014) on average, although a range of values have been proposed (–0.5 – –3.9 MPa/K: Litasov et al., 2005; Hernández et al., 2015). The transition is thought to impede mass transfer, perhaps leading to ponding of warm upwellings and stagnation of downgoing slabs (e.g., Tosi & Yuen, 2011; Fukao et al., 1992). However, a significant proportion of the upper mantle and MTZ may be composed of majorite garnet, which undergoes a transition to bridgmanite in the depth interval ∼640–750 km. Garnet is thought to be particularly stable in warm and basaltic environments (Xu et al., 2008). The majorite transition is described by a positive Clapeyron slope of ∼+1.3 MPa/K and therefore promote mass transfer (Hirose, 2002). Due to competing effects of both the olivine and garnet transitions, the d660 discontinuity may display greater topography and complexity than the d410, sometimes manifesting as two peaks within RFs (e.g., Andrews & Deuss, 2008). Consequently, it also possesses powerful diagnostic potential for both temperature and compositional variation, particularly within upwellings (Deuss, 2007; Jenkins et al., 2016).

Despite the typically well-mixed nature of the mid-to-lower mantle, within the depth interval 800–1200 km, impedance contrasts have been observed by multiple seismic methods (Kaneshima, 2016; Jenkins et al., 2017; Waszek et al., 2018). These discontinuities likely result from heterogeneity introduced by downgoing slabs or upwelling plumes, often linked to the presence of an entrained basaltic component (Kaneshima, 2016; Jenkins et al., 2017). A number of phase transitions within subducted material have been proposed, yet only a transition from stishovite to post-stishovite (e.g., Nomura et al., 2010) can occur outside of subduction settings. Therefore this phase transition has been invoked to explain observations of converted arrivals from mid-mantle depths below Iceland (Jenkins et al., 2017) and southern Africa (e.g., Vinnik et al., 2010). Intermittent observations of mid-mantle discontinuity structure can therefore be indicative of chemically distinct plume material, or small-scale entrained heterogeneity from a chemically distinct deep source. The mineral physics and seismological contributions discussed above provide the framework within which to interpret mantle upwellings and associated processes causing heterogeneous discontinuity structure below the African plate.

1.3 Previous Geophysical Observations of African Mantle Discontinuities

The African continent is the ideal locale to study mantle upwellings because it has remained largely free of collisional tectonics for over 550 Myr (Stern, 2004). Underlying subducted slabs are therefore largely restricted to the lower-most mantle (e.g., Steinberger, 2000). Furthermore, the relatively stationary nature of the African plate since 30 Ma (Gordon & Jurdy, 1986; Müller et al., 2015) presents the opportunity to

investigate the uncertain role of directly underlying mantle thermochemical anomalies in the formation of uplifted plateaus, rift and flood basalt related magmatism in the east (e.g., Pik et al., 2003; Pik et al., 2008; Rooney, 2017), the enigmatic CVL in the west (e.g., Ebinger & Sleep, 1998; King & Ritsema, 2000; Milelli et al., 2012), and volcanic provinces of Madagascar (e.g., Cucciniello et al., 2017).

Because sampling of African mantle discontinuity structure by reflected phases is piecemeal by nature (e.g., Huang et al., 2019; Day & Deuss, 2013), previous discontinuity observations are primarily derived from converted seismic phases. Prior African broad-scale converted phase studies utilized single station RF stacks. For example, Julià and Nyblade (2013) found intermittent observations of the wadsleyite to ringwoodite transition at ~520 km depth with little correlation with thermal or compositional proxies. Meanwhile, Tauzin et al. (2008) observed little correlation between MTZ thickness and sites of upwelling mantle across Africa.

A number of RF studies have focused on the MTZ structure below the northern East African Rift, centered around Ethiopia and Afar. Nyblade et al. (2000) used single station RF stacks to propose a normal MTZ thickness below Afar, suggesting that any small positive thermal anomaly (100–150 K) is isolated in the upper mantle. By contrast, Benoit et al. (2006) imaged an uplifted d660 by ~20–30 km below the eastern Ethiopian plateau but average values below the northwestern Ethiopian plateau, instead suggesting that a thermal anomaly of ~300 K restricted to central and eastern Ethiopia may extend below 660 km. Cornwell et al. (2011) revealed a regionally depressed d410 by 30–40 km below the Main Ethiopian Rift (MER) and Afar indicating a positive thermal anomaly of ~250 K in the MTZ. This study also observed variable d660 depths and interpreted these in light of compositional variations; Olivine-dominant below Afar, and garnet dominant below the MER. More recent MTZ studies imaged largely average MTZ thicknesses in Afar and central Ethiopia suggesting minimal thermal perturbations (Thompson et al., 2015; Reed, Gao, et al., 2016). These studies focused on local heterogeneity to invoke a stable melt layer caused by hydrous upwelling directly above the d410 in Afar (Thompson et al., 2015) and 20 km of MTZ thinning as evidence for a lower mantle plume stem isolated to below the western Ethiopian plateau (Reed, Gao, et al., 2016).

In the southern East African Rift, a thinned MTZ (30–40 km) and associated 200–300 K anomaly below the eastern rift branch is often interpreted as evidence for active upwelling from deeper mantle (Owens et al., 2000; Mulibo & Nyblade, 2013; Sun et al., 2017). Normal thickness MTZ below the western rift branch and Tanzanian craton is inconsistent with present-day thermal anomalies rooted at/below the MTZ (e.g., Sun et al., 2017). A significantly depressed d410 beneath rifts in Kenya and northern Tanzania (30–40 km) combined with a pervasively depressed d660, was interpreted as evidence for a warm, garnet dominant MTZ by Huerta et al. (2009). Mulibo and Nyblade (2013) suggested that processing RFs using 3D time-to-depth corrections leads to improved d660 depths compared to previous results, instead citing an uplifted d660 as compelling evidence for a connection of the African Superplume through the MTZ in this region.

Below southern Africa, while some small-scale discontinuity heterogeneity has been proposed (e.g., Blum & Shen, 2004; Vinnik et al., 2009), a consensus is emerging that there is minimal thermal perturbation of the MTZ below cratonic regions and the most southerly African rifts (Gao et al., 2002; Yu et al., 2015; Reed, Liu, et al., 2016; Sun et al., 2018). Elsewhere below the Cameroon Volcanic Line, Reusch et al. (2011) used MTZ RFs to suggest that thermal anomalies associated with magmatism are isolated to the upper mantle.

Particularly below regions of African Cenozoic magmatism, where reliable 3D time-to-depth corrections are paramount, quantitative comparisons between previ-

ous studies are hindered by the variable methodological approaches used in time-to-depth corrections and RF stacking, limited exploration of uncertainties in discontinuity depths and a lack of published data sets available electronically. We address these issues by applying a consistent, reproducible data processing approach at the continental-scale which facilitates quantitative interrogation of discontinuity depths and make our codes, data set and results available electronically. Furthermore, we allow more smoothing in our stacking procedure than previous regional studies, taking an approach to map and interpret broader-scale features away from the edges of our data coverage. Because previous studies lack agreement on the nature of the d660 discontinuity across Africa, we pay particular attention to this discontinuity in our study.

2 Data and Methods

2.1 P-to-s Receiver Functions

Upon encountering an impedance contrast, seismic energy undergoes partial conversions from P-to-s and vice versa. We refer to the P-to-s conversions from the MTZ discontinuities as P410s and P660s. Pds phases are delayed with respect to the direct-P phase arrival due to slower S-wave propagation above the discontinuity. In the absence of dipping interfaces and significant anisotropy, Pds arrivals can be enhanced through deconvolution of the vertical from the radial seismogram producing receiver functions (RFs). This process removes the effect of the seismic source, instrument response and source side structure, with the resulting time series representing Earth structure along the raypath beneath the seismometer. RFs can subsequently be stacked to further enhance arrivals. We calculate RFs using the time domain iterative deconvolution method of Ligorrìa and Ammon (1999) using up to 200 Gaussian pulses of a user defined width. This is initially set to 5 s (i.e. a maximum frequency of 0.2 Hz), but we also explore the effect of increasing maximum frequency in later analysis.

2.2 Seismic Data Processing

Our data download, processing and analysis is conducted using ObsPy (Beyreuther et al., 2010). Seismic data were sourced from the Incorporated Research Institutions for Seismology (IRIS), GeoForschungZentrum datacenter (GEOFON), French national datacenter (RESIF) and Institut de Physique du Globe de Paris datacenter (IPGP). Due to the lack of proximal tectonic environments generating large magnitude earthquakes over a broad backazimuthal range required for RF analysis, we extend our data coverage by calculating RFs not just from direct-P phases but also from PP and PKP phases. We use minimum earthquake magnitudes of 5.0 M_w, 6.2 M_w and 6.2 M_w at epicentral distance ranges of 30°–90°, 100°–130° and 145°–155° for P, PP and PKP RFs respectively. We consider phases recorded at stations throughout Africa active in the time period 1990–2019.

Initially raw data are windowed from 25 s before, to 150 s after, the direct phase arrival, filtered from 0.01–0.2 Hz and RFs with a 0.2 Hz maximum frequency are calculated. The quality control (QC) steps detailed below are used to assess this initial data set. RFs that pass QC criteria are recomputed using a range of higher maximum frequencies (0.5–0.9 Hz), which are re-assessed against the same QC to check that RFs also pass at the higher frequency. We follow the strict QC procedures adopted by Cottaar and Deuss (2016) but make a few minor adaptations. We exclude RFs in which the direct phase arrival does not occur within 2 s of zero (implying poor correlation between radial and vertical seismograms) and that when reconvolved with the vertical component reproduce less than 60% of the radial component seismogram. RFs are also removed in which pre- and post-peak amplitudes are greater than 40% and 70% of the direct phase arrival amplitude respectively. Lastly we impose signal-

to-noise ratio (SNR) constraints on the vertical (SNR>2.5) and radial (SNR>1.75) component seismograms used in RF calculation. We define SNR as $\frac{A_{signal}}{A_{noise}}$. A_{signal} is the root-mean squared amplitude for a 60 s window beginning at the direct phase arrival time using the ak135 reference model (Kennett et al., 1995). We include a preceding 5 s buffer and define A_{noise} as the root-mean squared amplitude for a 60 s window beginning 65 s before the predicted direct phase arrival time. Due to the strict nature of this automated QC procedure and the prevalence of sub-optimally deployed temporary networks yielding low SNR waveforms across Africa, we also employ a visual data inspection. Those vertical and radial component data that only failed QC through the SNR constraint are visually inspected when SNR values are greater than 1.25 for both components which resulted in the recovery of a further 2971 good Pds, PPds and PKPds RFs.

Supplementary Figures S1–S3 show stacks of Pds, PPds and PKPds RFs sorted by epicentral distance. Abundant interference from upper mantle and core diffracted phases with converted phases from MTZ discontinuities is visible at the limits of our initial epicentral distance ranges. We therefore further restrict the data used in subsequent stacking procedures to the ranges 40°–90°, 100°–125° and 145°–150° for the Pds, PPds and PKPds data sets respectively. This process yields 15020 Pds RFs, 12713 PPds RFs and 741 PKPds RFs (28474 RFs in total) from 2778 unique events recorded at 947 stations across Africa. Where appropriate, we also utilize RF stacking in the slowness domain to differentiate between multiples and conversions which have shallower and steeper incidence angles respectively, compared to the direct phase. Slowness stacks for the entire data set and for the five notable sub-regions across Africa can be found in Supplementary Figures S4 and S5.

2.3 Time-to-Depth Corrections

At a given epicentral distance, the travel-time difference between the direct phase and P-to-s converted phases depends on the depth to the discontinuity and the wavespeed difference between the P and S phases above it. To extract discontinuity depths from delay times of converted phases, we must assume a mantle wavespeed structure. Previous African MTZ RF studies primarily used 1D reference Earth models such as ak135 (Kennett et al., 1995) or regional relative arrival-time tomographic models that place no constraint on the background mean velocity structure. Without adequately accounting for 3D absolute wavespeed structure, reliable interpretations from MTZ studies are restricted to MTZ thickness, typically less influenced by overlying velocities than absolute discontinuity depths. Conversely insights into both the thermal and chemical nature of the MTZ can be obtained by interpreting the behavior of the d410 and d660 separately. We therefore seek reliable absolute discontinuity depths, necessitating consideration of 3D absolute wavespeed structure.

Here, we compute time-to-depth corrections using the 1D radial model ak135 (Figures S6–S8) and five 3D mantle absolute wavespeed models. We utilize the most up-to-date P- and S-wavespeed models for Africa (AFRP20 and AF2019: Boyce et al., 2021; Celli et al., 2020). Both AFRP20 and AF2019 are parameterized globally to ≥660 km depth and specifically improve resolution beneath Africa by including data from temporary deployments across the continent. We also test three recent global S-wavespeed models (SL2013SV, SEMUCB-WM1 and SGLOBErani: Schaeffer & Lebedev, 2013; French & Romanowicz, 2014; Chang et al., 2015). We calculate estimated S-wavespeed anomalies for the AFRP20 model by using the relationship $\delta V_S = \delta V_P \times (depth/2891 + 2)$ and use the inverse relationship to calculate estimated P-wavespeed anomalies for S-wavespeed models. Our 3D depth corrections account for station elevations and the continental crust appropriate for each tomographic model. We use the results from the five 3D time-to-depth corrections to quantitatively assess the uncertainties in MTZ discontinuity depths (Figures S9–S13).

2.4 Common Conversion Point Stacking

Raypath backazimuthal variation facilitates sampling of the MTZ over a broad area beneath a seismograph station ($\sim$500 km radius). Converted ray piercing points at 410 km depth for our African data set are shown in Figure 1. We employ the common conversion point stacking method of Dueker and Sheehan (1997) to account for the spread of conversion points beneath each station and enhance converted phase amplitudes. We define a grid of points spaced 0.5° in latitude and longitude and 2 km in depth throughout our study region (36°S–27°N, 0°E–52°E 60–1300 km depth). RF energy is back-propagated along raypaths and stacked into proximal grid points at distances within two-times the Fresnel-zone half width (Δ^{HW}) from the raypath using a normalized cubic spline weighting function defined by Lekić et al. (2011). The Fresnel zone half width is defined as:

$$\Delta^{HW} = \sqrt{(\frac{\lambda}{3} + z)^2 - z^2} \tag{1}$$

where λ is the wavelength of a 10 s shear wave and z is depth. Summed stacking weights and the standard error are tracked throughout the grid volume and are subsequently used to normalize stacked amplitudes and highlight poorly constrained regions within the grid (following Cottaar & Deuss, 2016). Supplementary Figure S6 shows the data coverage through the final summed stacking weights in the grid at 410 km and 660 km depth. We can expect to constrain discontinuities in regions where the summed weight is above 2 and amplitudes are greater than twice the standard error from the mean. Given these criteria, depths of peak amplitudes within the CCP stacks are picked in the ranges 370–450 km and 620–700 km to highlight converted phases arriving from mantle transition zone depths. We limit our presentation of CCP stacking results to these regions shown on map plots and highlight picked depths as yellow dashes in cross sections plots (Figures 2-6). We refer to 3D time-to-depth corrected CCP stacks based on the tomographic model used as AFRP20-CCP, AF2019-CCP, SL2013-CCP, SEMUCB-CCP and SGLOBErani-CCP throughout the manuscript. In the Supplementary Material, following van Stiphout et al. (2019), we quantitatively assess the observed topography in the different 3D time-to-depth corrected CCP stacks (Figures S14–S17) as well as a stack for ak135 (ak135-CCP). Strong positive correlation between MTZ discontinuity topography typically indicates inadequate account of upper mantle wavespeed structure, which is expected to vary significantly below Africa (e.g., Celli et al., 2020; Boyce et al., 2021). AFRP20-CCP achieves the best statistical performance of the resulting depths and is most similar to the average of the five 3D time-to-depth corrected CCP stacks (Figures S9–S12), so is the primary focus of results and interpretations below.

3 Results

3.1 MTZ Topography and Thickness

African MTZ discontinuity topography and thickness from AFRP20-CCP is explored in maps (Figures 2, 3) and cross section (Figure 4). By using five 3D tomographic models for time-to-depth corrections, we can isolate robust features of our CCP stacks, independent of the tomographic model used (Figures 5, S9–S10) and derive regional uncertainty estimates from the standard deviation of the d410 depth, d660 depth and MTZ thickness (Figures S11–S12). The average uncertainties across Africa are 4.3 km, 6.8 km and 3.9 km for d410 depth, d660 depth and MTZ thickness respectively. We highlight regions where AFRP20-CCP differs significantly from the average values across the five 3D time-to-depth corrected CCP stacks. We present discontinuity depths using a discrete color scales of 5 km for all map plots in line with quantitative uncertainties.

Below Ethiopia (ETH), the regional d410 depth is depressed at ∼417±5.0 km with maximum depths of ∼420–435 km below the Main Ethiopian Rift (MER), adjacent rift flanks and Afar (Figures 2, 4). Western ETH displays normal d410 and d660 depths. Regional d660 depths in AFRP20-CCP are ∼657±7.2 km, yet below the MER and eastward, d660 depths are ∼645–655 km. However, the average d660 depths across the five 3D time-to-depth corrected CCP stacks favors a depressed d660 in the southeast (Figures S10–S11). ETH shows a regional MTZ thickness of ∼240±3.4 km with strongest thinning of ∼25–30 km below Afar, the MER, adjacent rift flanks and in the southwest, while the northwestern Ethiopian plateau shows normal MTZ thickness (Figures 3, 5). Below the southern East African Rift (EAR), AFRP20-CCP shows a depressed regional d410 of ∼421±4.1 km depth with maximum depressions of >30 km in the northeast (Figures 2, 4). The regional d660 depth below EAR is also depressed at ∼667±5.8 km, with much of the region exhibiting ∼10 km depression of the d660. EAR displays a regional MTZ thickness of ∼244±3.0 km with the strongest zones of thinning (>20 km) confined to the northeast (Figures 3, 5).

Below southern Africa (SAF), the regional d410 depth is ∼407±3.9 km, while the regional d660 depth in AFRP20-CCP of ∼663±6.4 km (Figures 2, 4) differs significantly from the average across five 3D time-to-depth corrected CCP stacks of ∼653 km (Figures S10–S11). MTZ thickness is ∼256±5.1 km below SAF. Madagascar (MAD) shows depressed regional d410 and d660 depths of ∼415±5.8 km and ∼669±10.5 km respectively (Figure 2), however stacking amplitude loss, incoherency or error increases towards the north likely contributing to significant uncertainty, particularly in d660 depths (Figures S10–S11). MAD displays some apparent thinning of the MTZ (>10 km) below the southern, central and northern zones (Figures 3, 5). None of the six CCP stacks show a coherently stacked d410 below Cameroon (CAM: Figures 2, S9). AFRP20-CCP shows a regional d660 depth of ∼671±7.7 km below CAM (Figure 2) but differs significantly from the average across the five 3D time-to-depth corrected CCP stacks of ∼658 km (Figures S10–S11).

Figures 6 and S18–S19 explore the sensitivity of d410 and d660 depths to RF maximum frequency. Across Africa, d410 depths are largely insensitive to RF frequency content (Figure S18). Below EAR, the d660 peak splits towards higher frequencies, causing variability in d660 depth picks. Maximum amplitude peaks in Fmax=0.2 Hz stacks show depths of greater than 665 km (Figures 6 – A). At higher frequency, the maximum amplitude peak is the shallower of the two peaks, resulting in picks at depths of less than 660 km (Figure 6 – B), while the marginally weaker peak occurs at depths around ∼680 km (Figure 6). Below ETH d660 depths do not exhibit significant sensitivity to RF maximum frequency because the depth to the maximum converted phase amplitude is consistently less than 660 km (Figure 6). Indeed the regional d660 depth for ETH at 0.2 Hz and 0.9 Hz maximum frequency is ∼657 km, while beneath EAR regional d660 depths decrease from 667–661 km with increasing maximum RF frequency.

3.2 Mid-mantle Observations

We further interrogate AFRP20-CCP for mid-mantle conversions, selecting peak amplitudes in the depth range 960–1100 km (Figure 7), based on the abundance of scatters previously observed away from subduction zone settings at these depths (e.g., Kaneshima, 2016; Jenkins et al., 2017). Because low amplitude seismic conversions from mid-mantle depths often suffer interference from multiples, we assess whether observed peaks in AFRP20-CCP are robust by returning to the RF data themselves to compute fifteen local depth and slowness stacks for both Pds and PPds data sets (Figures S20–S29). Only well-sampled regions are chosen to maximize the data within each local stack that indicate similar discontinuity depths. Following Jenkins et al. (2017), we adopt a traffic-light system indicating our confidence that a seismic con-

version represents mid-mantle structure rather that an interfering multiple, where red indicates low confidence, yellow indicates medium confidence and green indicates high confidence. Our approach focuses on confirming the identification of mid-mantle conversions; we cannot confirm or deny the presence of mid-mantle conversions away from good data coverage.

Robust conversions appear below EAR at a depth of ∼1025 km and below southern Africa at ∼1056 km (R8, R15 - Figure 7). The corresponding high confidence Pds depth and slowness stack for region R8 is shown in Figure 8. EAR hosts a number of other regions with possible observations at 1018–1080 km depth (R5, R6, R7, R9, R10). We note that in our broader regional stacks (Figures S4 and S5), the EAR stack including 2902 RFs is the only stack to indicate a robust mid-mantle conversion, suggesting a discontinuity might be more widespread here. Possible mid-mantle conversions may also exist in R3, R12 and R13 below ETH and MAD respectively. Elsewhere, although positive amplitude peaks exist in AFRP20-CCP above two standard error, these are more likely the result of multiples from shallow structure (see slowness stacks in Figures S20–S29).

4 Discussion

4.1 Robustness of Discontinuity Depths

Significant differences in discontinuity depths between 3D time-to-depth corrected CCP stacks, computed using identical RF data (i.e. the same maximum frequency content), result directly from the 3D tomographic corrections applied, and are the primary source of uncertainty in our MTZ discontinuity depths. 3D time-to-depth corrections are further influenced by our imposed relationship between δV_S and δV_P, variable data coverage, resolving power, and inherent sampling differences between shear and compressional wavespeed tomographic models. Straightforward assessment of uncertainties in tomographic models is challenging. However, tomographic models typically underestimate wavespeed anomaly amplitudes leading to under correction of discontinuity depths in time-to-depth corrections. In this instance, discontinuities are not shifted shallow/deep enough so appear deeper/shallower than their true depth (see detail in Supplementary Material and Figures S14–S17). Quantitative analysis (see Supplementary Material) shows that our 3D time-to-depth corrections within CCP stacks remove a large degree of the correlated discontinuity topography present in ak135-CCP, where both MTZ discontinuities are strongly uplifted below SAF and strongly depressed below EAR and ETH (Figures S9–S10). Before interpreting discontinuity topography, we discuss the extent of under-or-over correction, and quantitatively consider the reliability of our discontinuity depth results.

Because previous studies in southern Africa find little thermal MTZ perturbation (e.g., Gao et al., 2002; Julià & Nyblade, 2013; Sun et al., 2018) below cool cratonic lithosphere (e.g., Celli et al., 2020; Boyce et al., 2021), we can test under-or-over correction of MTZ topography within 3D time-to-depth corrected CCP stacks beneath SAF and extend these inferences throughout other well sampled regions of Africa. For example, within AF2019-CCP, similar to ak135-CCP, regional d410 and d660 depths (∼399 km and ∼645 km) are uplifted below SAF, and are therefore likely under corrected in this region (Figures 4, S9–S10). Conversely in AFRP20-CCP, uplifted regional d410, but the slightly depressed regional d660 below SAF (∼407 km and ∼663 km) suggests that d410 depths are under corrected while the d660 depths may be slightly over corrected. These inferences are consistent with damped least-squares tomographic models constrained predominantly by shallowly penetrating shear waves in AF2019 resulting in lateral smearing, and deep diving compressional waves in AFRP20 resulting in vertical smearing (Celli et al., 2020; Boyce et al., 2021).

3D time-to-depth corrections, in regions where the upper mantle wavespeed is slow, shift apparent MTZ discontinuity depths shallower (e.g., Figure S14). Accounting for potential under correction of d410 depths in both AFRP20-CCP and AF2019-CCP would reduce the depression of the d410 below EAR and ETH. For the d660, accounting for under correction within AF2019-CCP and slight over correction within AFRP20-CCP leads to convergence of depth estimates (improved similarity across Figures 4b–d, S10), showing a depressed d660 beneath EAR and an uplifted d660 beneath ETH. Because the regional d660 discontinuity depths derived from the average of the five 3D time-to-depth corrected CCP stacks below ETH and EAR are slightly uplifted and depressed respectively (658.6 km and 665.8 km), this observation is likely robust rather than an artifact of our 3D wavespeed corrections. Additionally under correction of the d410 and over correction of the d660 could result in artificial MTZ thinning below areas of warm upper mantle anomalies. However, the normal MTZ thickness observed below the northwest Ethiopian plateau provides confidence that this effect is negligible below well instrumented regions.

The imposed relationship between δV_S and δV_P anomalies used in time-to-depth correction may also be a significant source of error, particularly in regions of highly heterogeneous upper mantle structure. One such region is the Main Ethiopian Rift (MER), in which a significant portion of the crust and upper mantle is melt rich (e.g., Kendall et al., 2005; Bastow et al., 2010). S-wavespeeds are significantly more sensitive to the presence of melt than P-wavespeeds (e.g., W. C. Hammond & Humphreys, 2000). Consequently when using the AFRP20 tomographic model, the imposed conversion to δV_S anomalies does not capture the full extent of slow S-wavespeed anomaly amplitudes observed along the MER in high resolution upper mantle studies ($\delta V_S \approx$ –11% Gallacher et al., 2016; Emry et al., 2019). Here, shallow mantle δV_S anomalies are $\approx 2.7 \times$ the highest δV_P anomaly in AFRP20. We estimate a melt rich upper 120 km below the MER may cause a further depression of up to 9 km on MTZ discontinuities. True discontinuity depths below the MER may therefore be shallower than imaged in AFRP20-CCP. While, melt is confined to a narrow region below the MER (e.g., Gallacher et al., 2016), our two Fresnel-zone half width smoothing criteria during CCP-stacking means this source of uncertainty may have a broader footprint at MTZ discontinuity depths. In the relatively melt poor southern EAR (Rooney, 2020), we expect this source of error to be less significant. Consequently, considering the distribution of melt in the upper mantle further supports the observed variable behavior of the d660 between ETH and EAR.

Furthermore, in the lower lithosphere of the Tanzanian craton ($\geq$90–135 km depth), AFRP20 shows P-wavespeed anomalies are slow (Boyce et al., 2021), while S-wavespeed anomalies remain fast to significantly greater depth ($\sim$175 km e.g., Weeraratne et al., 2003; Adams et al., 2012; Emry et al., 2019). If δV_S and δV_P anomalies are anti-correlated in this region, our assumed scaling between them breaks down. However the resulting estimated uncertainty is less than the vertical resolution (2 km) of our CCP stacks when using the AF2019 tomographic model (Celli et al., 2020).

To minimize the impact of data noise in our CCP stacks, we limit our interpretations to broad regional features, rather than shorter wavelength features at the edge of data coverage. To avoid miss-identification of maximum amplitude peak in a given depth interval which may not be derived from the true discontinuity depth, we only report discontinuity depths from the low frequency stacks (up to 0.2 Hz) that do not exhibit double peaked arrivals. In the cases where high frequency stacks exhibit a double peaked nature we take the utmost care when interpreting discontinuity depths.

4.2 MTZ Discontinuity Structure Below Africa

4.2.1 African MTZ Thickness

Our results show a strong correlation exists between locations of African Cenozoic magmatism and a locally thinned MTZ, particularly beneath ETH and EAR (Figures 3, 5), in contrast with results from the broad-scale study of Tauzin et al. (2008). Extending our observed correlation to regions at the edge of our data coverage across Cameroon, northern Madagascar, southwest ETH and western EAR may be less robust however (see Sections 4.2.4–4.2.5, Figures S11–S12). MTZ thinning of ∼25–30 km occurs below Afar and extends to the southwest below the MER and adjacent rift flanks, while the northwestern Ethiopian plateau is not underlain by a significantly thinned MTZ. Our results conflict with previous RF studies that suggest MTZ thinning is restricted to beneath the northwestern Ethiopian plateau (Reed, Gao, et al., 2016), the MTZ thickens towards the southwest (Cornwell et al., 2011) or observe little MTZ thinning throughout ETH (Nyblade et al., 2000; Thompson et al., 2015). Only the work of Cornwell et al. (2011) and Thompson et al. (2015) consider the impact of 3D absolute wavespeed heterogeneity on discontinuity depths beneath ETH (using the tomographic model of Montelli et al., 2006). However, our results migrated from time-to-depth using five different tomographic models show broad agreement beneath ETH (Figure 5).

MTZ thinning of >20 km also underlies northeastern EAR although magmatism occurs significantly offset to the east of the thinned MTZ (Figures 3, 5). Because strong cratonic lithosphere may extend beyond the mapped surficial Archean terranes (e.g., Figure 3), this offset may indicate deflection of upwelling material around the Tanzanian craton (Mulibo & Nyblade, 2013). Our results broadly agree with previous studies that have suggested MTZ thinning below northeast Tanzania and the eastern rift branch of the EAR reflects active upwelling while the lack of distinct thinning on western rift shows upwelling is likely to be more passive (Owens et al., 2000; Mulibo & Nyblade, 2013; Sun et al., 2017). MTZ thinning largely underlying Cenozoic magmatism in Afar, the MER and Kenyan eastern rift branch implies that magmatism is influenced by processes at MTZ depths or below. Elsewhere, below SAF, the average MTZ thickness across the five 3D time-to-depth corrected CCP stacks corroborates previous results (Gao et al., 2002; Yu et al., 2015; Reed, Liu, et al., 2016; Sun et al., 2018) indicating little MTZ thickness perturbation beneath this region but is subject to significant uncertainty (Figure S12).

4.2.2 African MTZ Temperature

Given robust MTZ discontinuity depths, MTZ temperature anomalies can be estimated using d410, d660 depths and MTZ thickness (e.g., Tauzin et al., 2008). We favor estimates based on d410 depths and MTZ thickness because d660 depths are sensitive to both temperature and composition (e.g., Deuss et al., 2006). Similarity between d410 depth and MTZ thickness derived temperature anomaly estimates indicates regional d410 depths obtained from 3D tomographic corrections are reliable, thermal anomalies traverse the MTZ and the d660 is not controlled by the garnet transition, i.e. a pyrolitic composition dominates. We calculate temperature estimates based on the depth to the maximum amplitude peak observed for both MTZ discontinuities within AFRP20-CCP for the lowest maximum frequency (up to 0.2 Hz), because thermal anomaly estimates based on higher maximum frequency CCP stacks yield variations over unrealistically short length-scales. While the absolute value and range of thermal anomaly estimates is highly sensitive to the Clapeyron slopes used to calculate them, the spatial pattern remains unchanged (in Figure 9 we assume average values: $\delta P/\delta T_{d410}$=3.0 MPa/K and $\delta P/\delta T_{d660}$=−2.5 MPa/K following Bina & Helffrich, 1994; Ye et al., 2014). Analysis presented in Section 4.1 suggests that these

thermal anomaly estimates are likely to represent an upper bound, because not all 3D wavespeed-induced topography may have been removed. By propagating a maximum regional d410 depth uncertainty of ∼5.8 km (in CAM, MAD) through the relationships used to estimate temperature anomalies, we anticipate uncertainties of <67 K using average Clapeyron slope values. The most sensitive Clapeyron slope would yield maximum uncertainties of >130 K.

In ETH, peak MTZ thermal anomalies below the MER and adjacent rift flanks are ∼100–150 K across both estimates, while below Afar, peak thermal anomalies vary from ∼150–275 K (Figure 9). The median MTZ thermal anomaly across ETH is slightly elevated ranging from ∼60–76 K. Further south beneath EAR, median thermal anomalies are significantly higher when using the d410 estimate (∼122 K) compared to the MTZ thickness proxy (∼35 K). Correspondingly, MTZ thicknesses predict a maximum thermal anomaly of ∼175 K in this region while the d410 depths predict >425 K. The differences between the two predictions may suggest the d660 in EAR is affected by non-olivine phase transitions (discussed further in the next Section). Evidence from our five CCP stacks and their corresponding 3D wavespeed models indicates that these observed differences are not likely the result of inaccurate 3D time-to-depth correction or thermal anomalies that do not traverse the MTZ. Median regional MTZ thermal anomalies for SAF are approximately equal across both estimates (Figure 9). We hesitate to interpret thermal anomalies in CAM and MAD where data coverage and thus results are highly variable.

Figure 9 shows that maximum MTZ temperature anomalies reside beneath EAR, and are significantly higher than those below ETH. Previous studies of the southern East African Rift consistently reveal a 200–350 K thermal anomaly below the eastern rift branch (Owens et al., 2000; Huerta et al., 2009; Mulibo & Nyblade, 2013; Sun et al., 2017) corroborated by our results. Meanwhile in Ethiopia previous studies do not provide a consensus on MTZ thermal anomalies because average MTZ thicknesses imaged by Nyblade et al. (2000); Thompson et al. (2015) and Reed, Gao, et al. (2016) below Afar and central Ethiopia suggest minimal thermal perturbations, while Benoit et al. (2006) and Cornwell et al. (2011) suggest significantly greater thermal perturbations of ∼250–300 K below central/eastern Ethiopia and Afar. We suggest that our observation of higher thermal anomalies in the MTZ below EAR compared to ETH is robust because both the d410 is deeper and MTZ thinner in EAR, compared to ETH, across the five 3D time-to-depth corrected CCP stacks (Figures S11–S12). At shallower depths, however, petrologically determined temperature estimates show the modest maximum temperature peak resides below ETH (+140 K at present beneath Afar: Rooney et al., 2012), and the slowest absolute upper mantle seismic wavespeeds (e.g., Boyce et al., 2021) exist below the MER and adjacent western Ethiopian plateau. In Section 4.4, we explore whether this anti-correlation between the location of highest temperatures in the East African upper mantle compared to the MTZ could be explained by additional heating of the Ethiopian upper mantle or a lateral influx of warm material to the Ethiopian upper mantle.

4.2.3 East African MTZ Composition

The depressed d410 underlain by an uplifted, frequency insensitive d660 below the MER and eastward (>10 km: Figures 2, 4, 6), indicates a warm MTZ dominated by phase transitions within the olivine system. Approximately average d660 depths below the adjacent western Ethiopian plateau indicate that the lower MTZ lacks significant thermal or compositional heterogeneity here (Figure 2). Both of these observations from AFRP20-CCP agree with prior work of Benoit et al. (2006). Unlike Cornwell et al. (2011), we do not observe any evidence for deepening of d660 depths to the southwest beneath ETH across the five 3D time-to-depth corrected CCP stacks (Figures S11–S12), and therefore do not interpret any compositional heterogeneity here.

Below EAR, the d410 depression of up to 30 km (Figures 2, 4), underlain by a depressed d660 at lower frequencies (>10 km: Figure 6 – A) with double-peaked arrivals at higher frequencies (Figure 6 – B), is consistent with a majorite garnet transition around the d660 (e.g., Deuss et al., 2006). The observed behavior of the d660, particularly at lower frequencies, agrees with prior work using RFs and reflected phase observations in EAR (Huerta et al., 2009; Day & Deuss, 2013). While Mulibo and Nyblade (2013) used 3D time-to-depth corrections from a relative arrival-time tomographic model to image an uplifted d660 in EAR, we suggest that depression of d660 in EAR is robust because it is consistently imaged across our five 3D time-to-depth corrected CCP stacks utilizing absolute wavespeed tomographic models (Figures S10–S11). The majorite garnet transition is expected to occur in anomalously warm regions (Hirose, 2002), corroborating the greater depression of the d410 observed below EAR than below ETH (Figures 2, 4). Both d660 depression (e.g., Jenkins et al., 2016) and double-peaked arrivals (e.g., Andrews & Deuss, 2008) have been interpreted as garnet signatures within upwellings elsewhere. Within Section 4.4 we investigate whether these two regions of differing MTZ behavior may indicate two mantle upwellings of distinct thermochemical nature lie beneath the East African Rift System.

4.2.4 Cameroon

The regional depth stack for Cameroon shows a weak converted arrival from the d410 (Figure S4). In the CCP stacks beneath Cameroon, the stacked d410 converted arrival is patchy and incoherent (Figures 2, S9), despite >500 piercing points sampling 410 km and 660 km depths, reasonable stacking weights (e.g., Figures 1, S6) and the ability to account for backazimuthal discontinuity topographic variations. This is all the more striking, as the d660 converted arrival has high amplitudes in depth, slowness and CCP stacks (Figures 2, S4, S10). However median d660 depths vary widely (649–671 km: Figures S10–11) and exhibit significant uncertainty, likely reflecting poorly resolved upper mantle wavespeeds away from dense seismic station coverage. Consequently we hesitate to interpret broad-scale d410 and d660 patterns beneath Cameroon.

The small coastal region, below which both d410 and d660 depths are reported, shows an apparently thinned MTZ by 20–30 km (Figures 3, 5, 10, S12), collocated with the most recent magmatism along the CVL at Mount Cameroon (Fitton & Dunlop, 1985) and the region of uncertain d660 depth observed by Reusch et al. (2011). High frequency CCP stack cross sections (Figure 10f – A) indicate double peaked behavior around both the d410 and d660 here, meaning multiple arrivals may interfere to produce depressions of both d410 and d660 in the low frequency stack (Figure 10e). Notably, very low positive d410 converted arrival amplitudes are often found below strong negative peaks (Figure 10b,e – B), but overlying negative arrivals do not appear to overprint any positive arrivals from the d410 within higher frequency stacks (Figure 10c,f). It remains unclear from slowness stacking whether these negative arrivals are multiples or conversions (Figure S4).

The normal amplitudes observed for the d660 converted arrival suggest the weak d410 converted arrival amplitudes are not due to incoherent stacking due to poor time-to-depth corrections. More appealing explanations for low d410 converted arrival amplitudes include a gradational discontinuity, incoherent stacking induced by short-wavelength discontinuity topography, or a low impedance contrast. A water-rich MTZ (e.g., Buchen et al., 2018) or basaltic accumulation (e.g., Kemp et al., 2019) have recently been invoked to explain decreased d410 impedance contrasts yet mechanisms to achieve this below the CVL are likely to require a lower mantle contribution. Reusch et al. (2011) found little evidence of MTZ thinning along the CVL, so favored a upper mantle thermal convection cell, adjacent to the Congo craton, as a causal mechanism for CVL magmatism. Regional tomographic models also do not support

a low wavespeed anomaly across the MTZ (Reusch et al., 2010; Adams et al., 2015), yet continental and global scale images do not rule out a lower mantle contribution to magmatism (e.g., French & Romanowicz, 2015; Emry et al., 2019; Boyce et al., 2021). The complex d410 and d660 behavior exhibited below Cameroon in this study is also not easily reconciled with a causal mechanism for the CVL solely isolated in the upper mantle, but improved data coverage in the region is required to draw more definite conclusions.

4.2.5 Madagascar

As far as we have been able to determine, this study is the first to illuminate MTZ discontinuity structure below Madagascar using converted phases. AFRP20-CCP reveals depressed median d410 and d660 depths with moderate MTZ thinning ($\sim$415 km, $\sim$669 km, $\sim$246 km respectively; Figures 2, 3, 10). Rather than interpret d410 depression and MTZ thinning at the northern and southern tips of Madagascar, we focus on central Madagascar where AFRP20 displays adequate upper mantle horizontal resolution (Boyce et al., 2021) and high-quality RF data coverage is good (Figures 10, S6).

Below central Madagascar, we observe a depression of both d410 and d660 ($\sim$10–15 km) centered at $\sim$17–19°S (Figures 2, 3, 10 – C). MTZ thinning and depression of both d410 and d660 in central Madagascar is observed across the majority of our five 3D time-to-depth corrected CCP stacks (Figures 5, S9–S10) although this region exhibits moderate uncertainties (Figures S11–S12). Similarly to EAR, depression of the d410 and d660 may indicate a warm upwelling crossing the MTZ in which the d660 is dominated by the garnet transition (e.g., Hirose, 2002), rather than the olivine transition. This is consistent with a relatively narrow slow wavespeed anomaly extending to >1000 km depth within AFRP20 (Boyce et al., 2021). While this may imply that central Madagascan Cenozoic magmatism is underlain by a mantle upwelling sourced below the MTZ, a significant thermal anomaly is not necessary to explain central Madagascan magmatism from a geochemical perspective (Cucciniello et al., 2017).

4.3 Implications of Mid-mantle Discontinuity Observations

Depth and slowness stacks indicate that EAR is underlain by several potential mid-mantle discontinuities, the most robust of which is observed at $\sim$1025 km depth in region R8 (Figures 7, 8, S5, S20–S29). Mid-mantle discontinuities below EAR are in a similar region to those identified using P'P' precursors (LeStunff et al., 1995). The region coincides with distinct slow wavespeeds within AFRP20 (Boyce et al., 2021) at $\sim$1000 km depth, which is the likely the mid-mantle expression of the African Superplume (Figures 7). Slow wavespeeds also correlate with intermediate confidence discontinuity observations below ETH and MAD at mid-mantle depths (regions R3, R12, R13).

SAF is also underlain by a high confidence result (R15), proximal to mid-mantle discontinuities previously identified using SKSdp RFs (Vinnik et al., 2010). However R15 does not correlate with slow wavespeeds at 800–1200 km depth in AFRP20 (Boyce et al., 2021), perhaps indicating other causal mechanisms beyond upwelling anomalous material need to be considered. Although the top of the African LLVP may underlie southern Africa, its is likely limited to below $\sim$1500 km depth (e.g., Ritsema et al., 2011; Cottaar & Lekić, 2016).

Several studies have suggested that the presence of mid-mantle discontinuities requires a basaltic component (e.g., Kaneshima, 2016; Jenkins et al., 2017), since phase changes are not predicted within a pyrolitic composition at mid-mantle depths (e.g., Murakami et al., 2005). To explain observations below both subduction zones

and regions of active upwelling, such as EAR and Iceland (e.g., Jenkins et al., 2017), chemical heterogeneity may be introduced to the mid-mantle by recycled basaltic crust that remains differentiated at the core mantle boundary, before subsequent entrainment within upwellings. Alternatively, upwellings may sample primordial material within LLVPs (Labrosse et al., 2007) introducing small-scale chemical heterogeneity to mid-mantle depths.

Association of high confidence mid-mantle discontinuities below EAR likely indicative of chemical heterogeneity associated with slow wavespeeds of the African Superplume (e.g., Ritsema et al., 2011; Boyce et al., 2021) corroborates previous studies (Ni et al., 2002; Simmons et al., 2007) that suggest the African Superplume is a thermochemical feature. East African magmatism may therefore be underlain by a basalt enriched or primordial chemically distinct upwelling. Slow mid-mantle wavespeeds demarcating a second whole mantle upwelling that reaches the lower mantle below the Indian Ocean (Boyce et al., 2021), distal from the African Superplume, are collocated with intermediate to low confidence mid-mantle discontinuity observations beneath ETH. Therefore an upwelling below ETH is not required to contain a chemically distinct component based on this mid-mantle criterion.

Elsewhere, intermediate confidence mid-mantle observations reside below offshore western and eastern Madagascar (R12, R13 - Figures 7, S20–S29). Lateral diversion of upwelling plume material in the depth range 1000–1500 km has been previously invoked, in the case of the Icelandic plume, to explain mid-mantle discontinuity observations below mainland Europe (Jenkins et al., 2017). .Within the AFRP20 tomographic model (Boyce et al., 2021), the slow wavespeeds below Madagascar ($\delta V_P < -0.6\%$) are distinct from a slow wavespeed conduit beneath the Reunion hotspot further east and do not extend directly down into the lower mantle much below $\sim$1000 km depth, so instead appear as an eastward extension the African Superplume. Intermediate confidence mid-mantle observations proximal to Madagascar may therefore result from sampling of chemically distinct material linked to the African Superplume, laterally diverted eastwards towards this region (e.g., Forte et al., 2010). Given that depressions of the d410 and d660 discontinuities below central Madagascan Cenozoic magmatism are collocated with slow wavespeeds extending from the upper mantle (e.g., Pratt et al., 2017) to $\sim$1000 km depth (Boyce et al., 2021), our intermediate confidence mid-mantle discontinuity observations cannot preclude the possibility that Madagascan magmatism is underlain by compositionally distinct upwelling material sourced from the African Superplume.

4.4 Implications for East African Magmatism

Although substantial debate has centered around the number of plumes that contribute to East African magmatism (e.g., George et al., 1998; Rogers et al., 2000; Furman, Bryce, et al., 2006; Nelson et al., 2012; Rooney, 2017), recent results point towards the contribution of two whole mantle plumes (Boyce et al., 2021): a subvertical slow wavespeed anomaly that extends eastward from the upper mantle below ETH to the lower mantle below the Indian Ocean and the African Superplume that extends southwestward from the upper mantle below the EAR to the lower mantle below southern Africa. Our RFs provide compelling evidence for a strong thermochemical upwelling below EAR likely associated with the African Superplume (Figure 11). By comparison, upwelling below central/eastern ETH is likely to be purely thermal in nature, exhibiting lower peak temperatures at MTZ depths. RF results alone are insufficient to independently confirm the two whole-mantle plume hypothesis due to relative proximity of upwellings at transition zone depths (Boyce et al., 2021) and reduction in data coverage below the Turkana depression separating the two distinct regions of MTZ behavior (Figure S6). However, a single broad plume is hard to reconcile with available RF evidence because a mechanism to heat the lower transition

zone below ETH without introducing a chemical perturbation from elsewhere is required. Both the garnet transition, dominant around the d660 in EAR and overlying d410 are predicted to promote mass transfer (Bina & Helffrich, 1994; Hirose, 2002) so ponding of hot material is not expected around MTZ depths, in agreement with available tomographic evidence (e.g., Boyce et al., 2021). Furthermore, lateral spreading of thermal anomalies within the transition zone is unlikely based on global observations (Lawrence & Shearer, 2008).

The nature of the d660 and mid-mantle discontinuities sampled here support the view that East African geochemical anomalies sourced in the deep mantle are likely transported to the surface via the basalt enriched African Superplume (e.g., Furman, Kaleta, et al., 2006). This upwelling likely taps the African LLVP (e.g., Cottaar & Lekić, 2016) and crosses the MTZ below EAR (e.g., Boyce et al., 2021). Entrainment of high $^3He/^4He$ ratios (R/Ra≈20 in Ethiopia: Marty et al., 1996; Pik et al., 2006; Hilton et al., 2011; Halldórsson et al., 2014) within a basalt enriched African Superplume is consistent with the developing consensus that only the most buoyant upwellings facilitate transport of primordial helium signatures to the surface (Williams et al., 2015; Jackson et al., 2017). This may be sourced from LLVPs in the lower mantle that likely host both recycled basalt and primordial helium signatures (Ballmer et al., 2016; Williams et al., 2019). The lack of significant along-rift variability in basalt isotopic ratios (e.g., Hilton et al., 2011; Halldórsson et al., 2014) suggests that Superplume material spreads throughout the East African upper mantle (Rooney, 2020). Consequently, significantly reduced seismic wavespeeds (Boyce et al., 2021) and modestly elevated petrologically-determined thermal anomalies (Rooney et al., 2012) below ETH compared to EAR, are challenging to explain by along-rift upper mantle compositional variation. Our results combined with those of Boyce et al. (2021) suggest compositionally anomalous material is presently not transported to the Ethiopian upper mantle directly from below because Ethiopia is underlain by a purely thermal anomaly likely sourced away from LLVPs in the lower mantle (Figure 11). Although Superplume material may be pervasive throughout the East African upper mantle, in Ethiopia specifically, conditions for mantle melting, rifting and highly anomalous upper mantle wavespeeds may be enhanced by the additional contribution of a purely thermal plume directly below. Proximal plumes of varying nature (e.g., Farnetani & Samuel, 2005) are therefore responsible for the complex East African upper mantle thermochemical signatures.

5 Conclusions

Using Pds, PPds, and PKPds receiver functions we present continent-wide observations of seismic discontinuity structure beneath Africa at mantle transition zone depths and below. We exploit a new high-resolution absolute P-wavespeed tomographic model for the African continent (Boyce et al., 2021) to migrate the RFs in our common conversion point stacks, and compare against results from four other S-wavespeed models.

A thin transition zone is seen beneath the majority of Cenozoic magmatism along the East African Rift, although some offset occurs and can be explained by interactions between upwellings and overriding stable mantle lithosphere. Our observations imply that East African Rift magmatism is influenced by processes at or below transition zone depths. The Main Ethiopian Rift and adjacent rift flanks are underlain by a depressed d410 (>10 km) while the uplifted d660 (∼10 km) is offset eastward, indicating a positive thermal anomaly in the Ethiopian transition zone. Below the eastern branch of the southern East African Rift, depression of the d410 of up to 30 km suggests a stronger thermal anomaly. Here, a regionally depressed (∼10 km) d660 showing frequency dependent splitting and robust mid-mantle discontinuities at ∼1025 km depth indicate an anomalous composition. Our observations combined with

slow wavespeeds illuminated by Boyce et al. (2021) suggest a hot, chemically distinct upwelling beneath the southern East African Rift, likely sourced from within the African LLVP. Meanwhile Ethiopian rift magmatism is underlain by a purely thermal upwelling, sourced away from the African LLVP. Variations in East African upper mantle seismic wavespeeds and petrologically determined temperature estimates can be reconciled with along-rift geochemical trends if the confluence of a dominant thermochemical African Superplume spreading in the upper mantle, with a purely thermal upwelling centered below Ethiopia is considered.

A patchy, incoherent d410 is underlain by a broadly coherent d660 below Cameroon. The complex d410 behavior, perhaps resulting from a regionally lowered impedance contrast, may suggest a causal mechanism for the Cameroon Volcanic Line not isolated to the upper mantle. Depression of MTZ discontinuities below central Madagascar collocated with tomographically imaged slow wavespeeds extending to ∼1000 km depth may reflect eastwards diversion of chemically distinct African Superplume material. However a direct causal link to Cenozoic Madagascan magmatism remains uncertain.

Acknowledgments

References

Adams, A. N., Nyblade, A. A., & Weeraratne, D. (2012). Upper mantle shear wave velocity structure beneath the East African plateau: evidence for a deep, plateauwide low velocity anomaly. *Geophys. J. Int.*, *189*(1), 123–142. doi: 10.1111/j.1365-246x.2012.05373.x

Adams, A. N., Wiens, D. A., Nyblade, A. A., Euler, G. G., Shore, P. J., & Tibi, R.

(2015). Lithospheric instability and the source of the Cameroon Volcanic Line: Evidence from Rayleigh wave phase velocity tomography. *J. Geophys. Res.*, *120*(3), 1708–1727. doi: 10.1002/2014jb011580

Akaogi, M., Ito, E., & Navrotsky, A. (1989). Olivine-modified spinel-spinel transitions in the system Mg_2SiO_4-Fe_2SiO_4: Calorimetric measurements, thermochemical calculation, and geophysical application. *J. Geophys. Res.*, *94*(B11), 15671–15685. doi: 10.1029/jb094ib11p15671

Andrews, J., & Deuss, A. (2008). Detailed nature of the 660 km region of the mantle from global receiver function data. *J. Geophys. Res.*, *113*(B6). doi: 10.1029/2007jb005111

Ballmer, M. D., Schumacher, L., Lekić, V., Thomas, C., & Ito, G. (2016). Compositional layering within the large low shear-wave velocity provinces in the lower mantle. *Geochem. Geophys. Geosyst.*, *17*(12), 5056–5077. doi: 10.1002/2016gc006605

Barruol, G., & Sigloch, K. (2012). *RHUM-RUM experiment, 2011-2015, (Réunion Hotspot and Upper Mantle – Réunion's Unterer Mantel)*. RESIF - Réseau Sismologique et géodésique Français. (Seismic Network) doi: 10.15778/RESIF .YV2011

Barry, P. H., Hilton, D. R., Fischer, T. P., Moor, J. M. d., Mangasini, F., & Ramirez, C. (2013). Helium and carbon isotope systematics of cold "mazuku" CO2 vents and hydrothermal gases and fluids from Rungwe Volcanic Province, southern Tanzania. *Chemical Geology*, *339*, 141–156. doi: 10.1016/j.chemgeo.2012.07.003

Bastow, I. D., Pilidou, S., Kendall, J.-M., & Stuart, G. (2010). Melt-induced seismic anisotropy and magma assisted rifting in Ethiopia: evidence from surface waves. *Geochem. Geophys. Geosyst.*, *11*. doi: 10.1029/2010GC003036

Benoit, M., Nyblade, A. A., Owens, T. J., & Stuart, G. (2006). Mantle transition zone structure and upper mantle S velocity variations beneath Ethiopia: Evidence for a broad, deep-seated thermal anomaly. *Geochem. Geophys. Geosyst.*, *7*(11), Q11013. doi: 10.1029/2006GC001398

Beyreuther, M., Barsch, R., Krischer, L., Megies, T., Behr, Y., & Wassermann, J. (2010). ObsPy: A Python Toolbox for Seismology. *Seis. Res. Lett.*, *81*(3), 530–533. doi: 10.1785/gssrl.81.3.530

Bina, C. R., & Helffrich, G. R. (1994). Phase transition Clapeyron slopes and transition zone seismic discontinuity topography. *J. Geophys. Res.*, *99*(B8), 15853. doi: 10.1029/94jb00462

Blum, J., & Shen, Y. (2004). Thermal, hydrous, and mechanical states of the mantle transition zone beneath southern Africa. *Earth Planet. Sci. Lett.*, *217*(3-4), 367–378. doi: 10.1016/s0012-821x(03)00628-9

Boyce, A., Bastow, I. D., Cottaar, S., Kounoudis, R., Guilloud De Courbeville, J., Caunt, E., & Desai, S. (2021). AFRP20: New P-wavespeed Model for the African Mantle Reveals Two Whole-Mantle Plumes Below East Africa and Neoproterozoic Modification of the Tanzania Craton. *Geochem. Geophys. Geosyst.*. doi: 10.1029/2020GC009302

Buchen, J., Marquardt, H., Speziale, S., Kawazoe, T., Ballaran, T. B., & Kurnosov, A. (2018). High-pressure single-crystal elasticity of wadsleyite and the seismic signature of water in the shallow transition zone. *Earth Planet. Sci. Lett.*, *498*, 77–87. doi: 10.1016/j.epsl.2018.06.027

Celli, N. L., Lebedev, S., Schaeffer, A. J., & Gaina, C. (2020). African cratonic lithosphere carved by mantle plumes. *Nat. Comms.*, *11*(1), 92. doi: 10.1038/s41467 -019-13871-2

Chang, S. J., Ferreira, A. M. G., Ritsema, J., van Heijst, H. J., & Woodhouse, J. H. (2015). Joint inversion for global isotropic and radially anisotropic mantle structure including crustal thickness perturbations. *J. Geophys. Res.*, *120*(6), 4278–4300. doi: 10.1002/2014jb011824

Chang, S. J., & Van der Lee, S. (2011). Mantle plumes and associated flow beneath Arabia and East Africa. *Earth Planet. Sci. Lett.*, *302*(3-4), 448–454. doi: 10 .1016/j.epsl.2010.12.050

Chorowicz, J. (2005). The East African rift system. *J. Afr. Earth Sci.*, *43*(1-3), 379–410. doi: 10.1016/j.jafrearsci.2005.07.019

Civiero, C., Hammond, J. O. S., Goes, S., Fishwick, S., Ahmed, A., Ayele, A., . . . Stuart, G. W. (2015). Multiple mantle upwellings in the transition zone beneath the northern East-African Rift system from relative P-wave travel-time tomography. *Geochem. Geophys. Geosyst.*, *16*(9), 2949–2968. doi: 10.1002/2015GC005948

Cornwell, D., Hetényi, G., & Blanchard, T. (2011). Mantle transition zone variations beneath the Ethiopian Rift and Afar: Chemical heterogeneity within a hot mantle? *Geophys. Res. Lett.*, *38*(16). doi: 10.1029/2011gl047575

Cottaar, S., & Deuss, A. (2016). Large-scale mantle discontinuity topography beneath Europe: Signature of akimotoite in subducting slabs. *J. Geophys. Res.*, *121*(1), 279–292. doi: 10.1002/2015jb012452

Cottaar, S., & Lekić, V. (2016). Morphology of seismically slow lower-mantle structures. *Geophys. J. Int.*, *207*(2), 1122–1136. doi: 10.1093/gji/ggw324

Courtillot, V., Davaille, A., Besse, J., & Stock, J. (2003). Three distinct types of hotspots in the Earth's mantle. *Earth Planet. Sci. Lett.*, *205*(3-4), 295–308. doi: 10.1016/s0012-821x(02)01048-8

Cucciniello, C., Melluso, L., Roex, A. P. l., Jourdan, F., Morra, V., Gennaro, R. d., & Grifa, C. (2017). From olivine nephelinite, basanite and basalt to peralkaline trachyphonolite and comendite in the Ankaratra volcanic complex, Madagascar: 40Ar/39Ar ages, phase compositions and bulk-rock geochemical and isotopic evolution. *Lithos*, *274*, 363–382. doi: 10.1016/j.lithos.2016.12.026

Davies, G. F. (1995). Penetration of plates and plumes through the mantle transition zone. *Earth Planet. Sci. Lett.*, *133*(3-4), 507–516. doi: 10.1016/0012 -821x(95)00039-f

Day, E. A., & Deuss, A. (2013). Reconciling PP and P'P' precursor observations of a complex 660 km seismic discontinuity. *Geophys. J. Int.*, *194*(2), 834–838. doi: 10.1093/gji/ggt122

De Plaen, R. S. M., Bastow, I. D., Chambers, E. L., Keir, D., Gallacher, R. J., & Keane, J. (2014). The development of magmatism along the Cameroon Volcanic Line: Evidence from seismicity and seismic anisotropy. *J. Geophys. Res.*, *119*(5), 4233–4252. doi: 10.1002/2013jb010583

Deschamps A., Déverchère, J., & Ferdinand, R. (2007). *Seismotanz'07.* RESIF - Réseau Sismologique et géodésique Français. (Seismic Network) doi: 10.15778/ RESIF.ZS2007

Deuss, A. (2007). Seismic observations of transition-zone discontinuities beneath hotspot locations. In *Plates, Plumes and Planetary Processes.* Geological Society of America. doi: 10.1130/2007.2430(07)

Deuss, A., Andrews, J., & Day, E. (2013). Seismic observations of mantle discontinuities and their mineralogical and dynamical interpretation. In *Physics and chemistry of the deep earth* (p. 295-323). John Wiley & Sons, Ltd. doi: 10 .1002/9781118529492.ch10

Deuss, A., Redfern, S. A. T., Chambers, K., & Woodhouse, J. H. (2006). The Nature of the 660-Kilometer Discontinuity in Earth's Mantle from Global Seismic Observations of PP Precursors. *Science*, *311*(5758), 198–201. doi: 10.1126/science.1120020

Deuss, A., & Woodhouse, J. (2001). Seismic Observations of Splitting of the Mid-Transition Zone Discontinuity in Earth's Mantle. *Science*, *294*(5541), 354–357. doi: 10.1126/science.1063524

Dueker, K. G., & Sheehan, A. F. (1997). Mantle discontinuity structure from mid-point stacks of converted P to S waves across the Yellowstone hotspot track. *J.*

Geophys. Res., *102*(B4), 8313–8327. doi: 10.1029/96jb03857

Dziewonski, A. M., & Anderson, D. L. (1981). Preliminary reference Earth model. *Phys. Earth Planet. Int.*, *25*(4), 297–356. doi: 10.1016/0031-9201(81)90046-7

Ebinger, C. J. (2007). *AFAR.* International Federation of Digital Seismograph Networks. (Seismic Network) doi: 10.7914/SN/ZE_2007

Ebinger, C. J. (2012). *Dynamics of the Lake Kivu System.* International Federation of Digital Seismograph Networks. (Seismic Network) doi: 10.7914/SN/YA_2012

Ebinger, C. J., & Sleep, N. (1998). Cenozoic magmatism throughout East Africa resulting from impact of a single plume. *Nature*, *395*, 788-791. doi: 10.1038/27417

Emry, E. L., Shen, Y., Nyblade, A. A., Flinders, A., & Bao, X. (2019). Upper Mantle Earth Structure in Africa From Full-Wave Ambient Noise Tomography. *Geochem. Geophys. Geosyst..* doi: 10.1029/2018gc007804

Fairhead, J. (1988). Mesozoic Plate Tectonic Reconstructions of the Central South Atlantic Ocean: The Role of the West and Central African Rift System. *Tectonophysics*, *155*(1-4), 181–191.

Farnetani, C. G., & Samuel, H. (2005). Beyond the thermal plume paradigm. *Geophys. Res. Lett.*, *32*(7). doi: 10.1029/2005gl022360

Fitton, J., & Dunlop, H. (1985). The Cameroon Line, West Africa, and its Bearing on the Origin of Oceanic and Continental Alkali Basalt. *Earth Planet. Sci. Lett.*, *72*(1), 23–38. doi: 10.1016/0012-821x(85)90114-1

Fontaine, F. R., Barruol, G., & Gonzalez, A. (2015). *Rivière des Pluies Project, La Réunion Island, 2015-2018.* RESIF - Réseau Sismologique et géodésique Français. (Seismic Network) doi: 10.15778/RESIF.ZF2015

Forte, A. M., Quéré, S., Moucha, R., Simmons, N. A., Grand, S. P., Mitrovica, J. X., & Rowley, D. B. (2010). Joint seismic–geodynamic-mineral physical modelling of African geodynamics: A reconciliation of deep-mantle convection with surface geophysical constraints. *Earth Planet. Sci. Lett.*, *295*(3-4), 329–341. doi: 10.1016/j.epsl.2010.03.017

French, S. W., & Romanowicz, B. (2014). Whole-mantle radially anisotropic shear velocity structure from spectral-element waveform tomography. *Geophys. J. Int.*, *199*(3), 1303–1327. doi: 10.1093/gji/ggu334

French, S. W., & Romanowicz, B. (2015). Broad plumes rooted at the base of the Earth's mantle beneath major hotspots. *Nature*, *525*(7567), 95–99. doi: 10.1038/nature14876

Fukao, Y., Obayashi, M., Inoue, H., & Nenbai, M. (1992). Subducting slabs stagnant in the mantle transition zone. *J. Geophys. Res.*, *97*(B4), 4809. doi: 10.1029/91jb02749

Furman, T., Bryce, J. G., Rooney, T. O., Hanan, B. B., Yirgu, G., & Ayalew, D. (2006). Heads and tails: 30 million years of the Afar plume. *Geol. Soc. Lond. Spec. Pub.*, *259*(1), 95–119. doi: 10.1144/GSL.SP.2006.259.01.09

Furman, T., Kaleta, K. M., Bryce, J. G., & Hanan, B. B. (2006). Tertiary Mafic Lavas of Turkana, Kenya: Constraints on East African Plume Structure and the Occurrence of High-μ Volcanism in Africa. *J. Petrol.*, *47*(6), 1221–1244. doi: 10.1093/petrology/egl009

Gaherty, J. B., & Ebinger, C. J. (2013). *Study of extension and magmatism in malawi and tanzania.* International Federation of Digital Seismograph Networks. (Seismic Network) doi: 10.7914/SN/YQ_2013

Gaherty, J. B., & Shillington, D. (2010). *2009 Malawi Earthquake RAMP Response.* International Federation of Digital Seismograph Networks. (Seismic Network) doi: 10.7914/SN/YI_2010

Gallacher, R. J., Keir, D., Harmon, N., Stuart, G., Leroy, S., Hammond, J. O. S., … Ahmed, A. (2016). The initiation of segmented buoyancy-driven melting during continental breakup. *Nature Communications*, *7*(1), 13110. doi:

10.1038/ncomms13110

Gao, S. S. (2009). *Four-Dimensional Anatomy of Continental Rifts Transitioning into Sea Floor spreading: Insights from Afar, Ethiopia for oil and gas exploration of global rift systems and passive continental margins.* International Federation of Digital Seismograph Networks. (Seismic Network) doi: 10.7914/SN/ZK_2009

Gao, S. S., & Liu, K. H. (2012). *Passive seismic study of early rifting in Botswana, Zambia, and Malawi.* International Federation of Digital Seismograph Networks. (Seismic Network) doi: 10.7914/SN/XK_2012

Gao, S. S., Silver, P. G., Liu, K. H., & Group, K. S. (2002). Mantle discontinuities beneath Southern Africa. *Geophys. Res. Lett.*, *29*(10), 129–1-129-4. doi: 10.1029/2001gl013834

George, R., Rogers, N. W., & Kelley, S. (1998). Earliest magmatism in Ethiopia: evidence for two mantle plumes in one continental flood basalt province. *Geology*, *26*, 923-926. doi: 10.1130/0091-7613(1998)026⟨0923:EMIEEF⟩2.3.CO;2

Gordon, R. G., & Jurdy, D. M. (1986). Cenozoic global plate motions. *J. Geophys. Res.*, *91*(B12), 12389–12406. doi: 10.1029/jb091ib12p12389

Halldórsson, S. A., Hilton, D. R., Scarsi, P., Abebe, T., & Hopp, J. (2014). A common mantle plume source beneath the entire East African Rift System revealed by coupled helium-neon systematics. *Geophys. Res. Lett.*, *41*(7), 2304–2311. doi: 10.1002/2014gl059424

Hammond, J. O. S., & Goitom, B. (2011a). *Eritrea Seismic Project.* International Federation of Digital Seismograph Networks. (Seismic Network) doi: 10.7914/SN/5H_2011

Hammond, J. O. S., & Goitom, B. (2011b). *Nabro Urgency Array.* International Federation of Digital Seismograph Networks. (Seismic Network) doi: 10.7914/SN/4H_2011

Hammond, W. C., & Humphreys, E. D. (2000). Upper mantle seismic wave velocity: Effects of realistic partial melt geometries. *J. Geophys. Res.*, *105*(B5), 10975–10986. doi: 10.1029/2000jb900041

Heit, B., Yuan, X., Jokat, W., Weber, M., & Geissler, W. (2010). *WALPASS Network, Namibia, 2010/2012.* Deutsches GeoForschungsZentrum GFZ. (Seismic Network) doi: 10.14470/1N134371

Helffrich, G. R. (2000). Topography of the transition zone seismic discontinuities. *Rev. Geophys.*, *38*(1), 141–158. doi: 10.1029/1999RG000060

Helffrich, G. R., & Wood, B. J. (1996). 410 km discontinuity sharpness and the form of the olivine $\alpha - \beta$ phase diagram: resolution of apparent seismic contradictions. *Geophys. J. Int.*, *126*(2), F7–F12. doi: 10.1111/j.1365-246x.1996.tb05292.x

Hernández, E. R., Brodholt, J., & Alfè, D. (2015). Structural, vibrational and thermodynamic properties of Mg 2 SiO 4 and MgSiO 3 minerals from first-principles simulations. *Phys. Earth Planet. Int.*, *240*, 1–24. doi: 10.1016/j.pepi.2014.10.007

Hilton, D. R., Halldórsson, S. A., Barry, P. H., Fischer, T. P., Moor, J. M. d., Ramirez, C. J., . . . Scarsi, P. (2011). Helium isotopes at Rungwe Volcanic Province, Tanzania, and the origin of East African Plateaux. *Geophys. Res. Lett.*, *38*(21). doi: 10.1029/2011gl049589

Hirose, K. (2002). Phase transitions in pyrolitic mantle around 670-km depth: Implications for upwelling of plumes from the lower mantle. *J. Geophys. Res.*, *107*(B4), ECV 3–1-ECV 3-13. doi: 10.1029/2001jb000597

Huang, Q., Schmerr, N., Waszek, L., & Beghein, C. (2019). Constraints on Seismic Anisotropy in the Mantle Transition Zone From Long-Period SS Precursors. *J. Geophys. Res.*, *124*(7), 6779–6800. doi: 10.1029/2019jb017307

Huerta, A. D., Nyblade, A. A., & Reusch, A. M. (2009). Mantle transition zone structure beneath Kenya and Tanzania: more evidence for a deep-seated

thermal upwelling in the mantle. *Geophys. J. Int.*, *177*(3), 1249–1255. doi: 10.1111/j.1365-246x.2009.04092.x

Jackson, M. G., Konter, J. G., & Becker, T. W. (2017). Primordial helium entrained by the hottest mantle plumes. *Nature*, *542*(7641), 340–343. doi: 10.1038/nature21023

Jenkins, J., Cottaar, S., White, R. S., & Deuss, A. (2016). Depressed mantle discontinuities beneath Iceland: Evidence of a garnet controlled 660 km discontinuity? *Earth Planet. Sci. Lett.*, *433*, 159–168. doi: 10.1016/j.epsl.2015.10.053

Jenkins, J., Deuss, A., & Cottaar, S. (2017). Converted phases from sharp 1000 km depth mid-mantle heterogeneity beneath Western Europe. *Earth Planet. Sci. Lett.*, *459*, 196–207. doi: 10.1016/j.epsl.2016.11.031

Julià, J., & Nyblade, A. A. (2013). Probing the upper mantle transition zone under Africa with P520s conversions: Implications for temperature and composition. *Earth Planet. Sci. Lett.*, *368*, 151–162. doi: 10.1016/j.epsl.2013.02.021

Kaneshima, S. (2016). Seismic scatterers in the mid-lower mantle. *Phys. Earth Planet. Int.*, *257*, 105–114. doi: 10.1016/j.pepi.2016.05.004

Katsura, T., Yamada, H., Nishikawa, O., Song, M., Kubo, A., Shinmei, T., . . . Funakoshi, K. (2004). Olivine-wadsleyite transition in the system (Mg,Fe)2SiO4. *J. Geophys. Res.*, *109*(B2). doi: 10.1029/2003jb002438

Keir, D., & Ebinger, C. J. (2014). *Southern Lake Tanganyika experiment.* International Federation of Digital Seismograph Networks. (Seismic Network) doi: 10.7914/SN/ZV_2014

Keir, D., & Hammond, J. O. S. (2009). *AFAR0911.* International Federation of Digital Seismograph Networks. (Seismic Network) doi: 10.7914/SN/2H_2009

Kemp, J., M.and Jenkins, Maclennan, J., & Cottaar, S. (2019). X-discontinuity and transition zone structure beneath Hawaii suggests a heterogeneous plume. *Earth Planet. Sci. Lett.*, *527*, 115781. doi: 10.1016/j.epsl.2019.115781

Kendall, J.-M., Stuart, G., Ebinger, C. J., Bastow, I. D., & Keir, D. (2005). Magma assisted rifting in Ethiopia. *Nature*, *433*, 146-148. doi: 10.1038/nature03161

Kennett, B. L. N., Engdahl, E. R., & Buland, R. (1995). Constraints on seismic velocities in the earth from traveltimes. *Geophys. J. Int.*, *122*(1), 108-124. doi: 10.1111/j.1365-246X.1995.tb03540.x

Keranen, K. (2013). *Exploring extensional tectonics beyond the ethiopian rift.* International Federation of Digital Seismograph Networks. (Seismic Network) doi: 10.7914/SN/YY_2013

King, S. D., & Ritsema, J. (2000). African Hot Spot Volcanism: Small-Scale Convection in the Upper Mantle Beneath Cratons. *Science*, *290*(5494), 1137–1140. doi: 10.1126/science.290.5494.1137

Labrosse, S., Hernlund, J. W., & Coltice, N. (2007). A crystallizing dense magma ocean at the base of the Earth's mantle. *Nature*, *450*(7171), 866–869. doi: 10.1038/nature06355

Lawrence, J. F., & Shearer, P. M. (2008). Imaging mantle transition zone thickness with SdS - SS finite-frequency sensitivity kernels. *Geophys. J. Int.*, *174*(1), 143–158. doi: 10.1111/j.1365-246x.2007.03673.x

Lekić, V., French, S. W., & Fischer, K. M. (2011). Lithospheric Thinning Beneath Rifted Regions of Southern California. *Science*, *334*(6057), 783–787. doi: 10.1126/science.1208898

Lemnifi, A. A., Browning, J., Elshaafi, A., Aouad, N. S., & Yu, Y. (2019). Receiver function imaging of mantle transition zone discontinuities and the origin of volcanism beneath Libya. *Journal of Geodynamics*, *124*, 93–103. doi: 10.1016/j.jog.2019.01.009

Leroy, S., Keir, D., & Stuart, G. W. (2009). *Young Conjugate Margins Lab in the Gulf of Aden.* International Federation of Digital Seismograph Networks. (Seismic Network) doi: 10.7914/SN/XW_2009

LeStunff, Y., Wicks, C. W., & Romanowicz, B. (1995). P'P' Precursors Under

Africa: Evidence for Mid-Mantle Reflectors. *Science*, *270*(5233), 74–77. doi: 10.1126/science.270.5233.74

Li, C., Van der Hilst, R. D., Engdahl, R., & Burdick, S. (2008). A new global model for P wave speed variations in Earth's mantle. *Geochem. Geophys. Geosyst.*, *9*(5). doi: 10.1029/2007GC001806

Ligorrìa, J., & Ammon, C. (1999). Iterative deconvolution and receiver-function estimation. *Bull. Seis. Soc. Am.*, *89*(5), 1395-1400.

Litasov, K., Ohtani, E., Sano, A., Suzuki, A., & Funakoshi, K. (2005). In situ X-ray diffraction study of post-spinel transformation in a peridotite mantle: Implication for the 660-km discontinuity. *Earth Planet. Sci. Lett.*, *238*(3-4), 311–328. doi: 10.1016/j.epsl.2005.08.001

Lithgow-Bertelloni, C., & Silver, P. (1998). Dynamic topography, plate driving forces and the African superswell. *Nature*, *395*(6699), 269-272. doi: 10.1038/26212

Marty, B., Pik, R., & Yirgu, G. (1996). Helium isotopic variations in Ethiopian plume lavas: nature of magmatic sources and limit on lower mantle contribution. *Earth Planet. Sci. Lett.*, *144*(1-2), 223–237. doi: 10.1016/0012-821x(96)00158-6

Melluso, L., Cucciniello, C., Roex, A. l., & Morra, V. (2016). The geochemistry of primitive volcanic rocks of the Ankaratra volcanic complex, and source enrichment processes in the genesis of the Cenozoic magmatism in Madagascar. *Geochimica et Cosmochimica Acta*, *185*, 435–452. doi: 10.1016/j.gca.2016.04.005

Milelli, L., Fourel, L., & Jaupart, C. (2012). A lithospheric instability origin for the Cameroon Volcanic Line. *Earth Planet. Sci. Lett.*, *335-336*, 80-87. doi: 10.1016/j.epsl.2012.04.028

Montelli, R., Nolet, G., Dahlen, F., & Masters, G. (2006). A catalogue of deep mantle plumes: new results from finite-frequency tomography. *Geochem. Geophys. Geosyst.*, *7*, Q11007. doi: 10.1029/2006GC001248

Mulibo, G. D., & Nyblade, A. A. (2013). Mantle transition zone thinning beneath eastern Africa: Evidence for a whole-mantle superplume structure. *Geophys. Res. Lett.*, *40*(14), 3562–3566. doi: 10.1002/grl.50694

Müller, R. D., Seton, M., Zahirovic, S., Williams, S. E., Matthews, K. J., Wright, N. M., . . . Cannon, J. (2015). Ocean Basin Evolution and Global-Scale Plate Reorganization Events Since Pangea Breakup. *Annual Review of Earth and Planetary Sciences*, *44*(1), 1–32. doi: 10.1146/annurev-earth-060115-012211

Murakami, M., Hirose, K., Sata, N., & Ohishi, Y. (2005). Post-perovskite phase transition and mineral chemistry in the pyrolitic lowermost mantle. *Geophys. Res. Lett.*, *32*(3). doi: 10.1029/2004gl021956

Nelson, W. R., Furman, T., van Keken, P. E., Shirey, S. B., & Hanan, B. B. (2012). OsHf isotopic insight into mantle plume dynamics beneath the East African Rift System. *Chemical Geology*, *320*(189), 66–79. doi: 10.1016/j.chemgeo.2012.05.020

Ni, S., Tan, E., Gurnis, M., & Helmberger, D. (2002). Sharp Sides to the African Superplume. *Science*, *296*(5574), 1850-1852. doi: 10.1126/science.1070698

Nomura, R., Hirose, K., Sata, N., & Ohishi, Y. (2010). Precise determination of post-stishovite phase transition boundary and implications for seismic heterogeneities in the mid-lower mantle. *Phys. Earth Planet. Int.*, *183*(1-2), 104–109. doi: 10.1016/j.pepi.2010.08.004

Nyblade, A. A. (2000). *Seismic Investigation of Deep Structure Beneath the Ethiopian Plateau and Afar Depression.* International Federation of Digital Seismograph Networks. (Seismic Network) doi: 10.7914/SN/XI_2000

Nyblade, A. A. (2007). *AfricaArray.* International Federation of Digital Seismograph Networks. (Seismic Network) doi: 10.7914/SN/ZP_2007

Nyblade, A. A. (2015). *Africaarray - namibia.* IRIS. (Seismic Network) doi: 10

.7914/SN/8A_2015

Nyblade, A. A., Knox, R., & Gurrola, H. (2000). Mantle transition zone thickness beneath Afar: implications for the origin of the Afar hotspot. *Geophys. J. Int.*, *142*, 615-619.

Owens, T. J., & Nyblade, A. A. (1994). *Seismic investigations of the Lithospheric Structure of the Tanzanian Craton.* International Federation of Digital Seismograph Networks. (Seismic Network) doi: 10.7914/SN/XD_1994

Owens, T. J., Nyblade, A. A., Gurrola, H., & Langston, C. A. (2000). Mantle transition zone structure beneath Tanzania, east Africa. *Geophys. Res. Lett.*, *27*(6), 827–830. doi: 10.1029/1999gl005429

Penn State University. (2004). *AfricaArray.* International Federation of Digital Seismograph Networks. (Seismic Network) doi: 10.7914/SN/AF

Pik, R., Marty, B., Carignan, J., & Lavé, J. (2003). Stability of the Upper Nile drainage network (Ethiopia) deduced from (U–Th)/He thermochronometry: implications for uplift and erosion of the Afar plume dome. *Earth Planet. Sci. Lett.*, *215*(1-2), 73–88. doi: 10.1016/s0012-821x(03)00457-6

Pik, R., Marty, B., Carignan, J., Yirgu, G., & Ayalew, T. (2008). Timing of East African Rift development in southern Ethiopia: Implication for mantle plume activity and evolution of topography. *Geology*, *36*(2), 167–170. doi: 10.1130/g24233a.1

Pik, R., Marty, B., & Hilton, D. (2006). How many mantle plumes in Africa? The geochemical point of view. *Chemical Geology*, *226*(3-4), 100–114. doi: 10.1016/j.chemgeo.2005.09.016

Pratt, M. J., Wysession, M. E., Aleqabi, G., Wiens, D. A., Nyblade, A. A., Shore, P., . . . Rindraharisaona, E. (2017). Shear velocity structure of the crust and upper mantle of Madagascar derived from surface wave tomography. *Earth Planet. Sci. Lett.*, *458*, 405–417. doi: 10.1016/j.epsl.2016.10.041

Reed, C. A., Gao, S. S., Liu, K. H., & Yu, Y. (2016). The mantle transition zone beneath the Afar Depression and adjacent regions: implications for mantle plumes and hydration. *Geophys. J. Int.*, *205*(3), 1756–1766. doi: 10.1093/gji/ggw116

Reed, C. A., Liu, K. H., Chindandali, P. R. N., Massingue, B., Mdala, H., Mutamina, D., . . . Gao, S. S. (2016). Passive rifting of thick lithosphere in the southern East African Rift: Evidence from mantle transition zone discontinuity topography. *J. Geophys. Res.*, *121*(11), 8068–8079. doi: 10.1002/2016jb013131

Reusch, A. M., Nyblade, A. A., Tibi, R., Wiens, D. A., Shore, P. J., Bekoa, A., . . . Nnange, J. M. (2011). Mantle transition zone thickness beneath Cameroon: evidence for an upper mantle origin for the Cameroon Volcanic Line. *Geophys. J. Int.*, *187*(3), 1146–1150. doi: 10.1111/j.1365-246x.2011.05239.x

Reusch, A. M., Nyblade, A. A., Wiens, D. A., Shore, P. J., Ateba, B., Tabod, C. T., & Nnange, J. M. (2010). Upper mantle structure beneath Cameroon from body wave tomography and the origin of the Cameroon Volcanic Line. *Geochem. Geophys. Geosyst.*, *11*(10), Q10W07. doi: 10.1029/2010gc003200

Ritsema, J., Deuss, A., Van Heijst, H., & Woodhouse, J. (2011). S40RTS: a degree-40 shear-velocity model for the mantle from new Rayleigh wave dispersion, teleseismic traveltime and normal-mode splitting function measurements. *Geophys. J. Int.*, *184*(3), 1223–1236. doi: 10.1111/j.1365-246X.2010.04884.x

Ritsema, J., Van Heijst, H., & Woodhouse, J. (1999). Complex shear wave velocity structure imaged beneath Africa and Iceland. *Science*, *286*, 1925-1928. doi: 10.1126/science.286.5446.1925

Rogers, N. W., Macdonald, R., Fitton, J., George, R., Smith, R., & Barreiro, B. (2000). Two mantle plumes beneath the East African rift system: Sr, Nd and Pb isotope evidence from Kenya Rift basalts. *Earth Planet. Sci. Lett.*, *176*, 387-400. doi: 10.1016/s0012-821x(00)00012-1

Rooney, T. O. (2017). The Cenozoic magmatism of East-Africa: Part I — Flood

basalts and pulsed magmatism. *Lithos*, *286-287*, 264 - 301. doi: https://doi .org/10.1016/j.lithos.2017.05.014

Rooney, T. O. (2020). The Cenozoic magmatism of East Africa: Part V – Magma sources and processes in the East African Rift. *Lithos*, *360-361*, 105296. doi: https://doi.org/10.1016/j.lithos.2019.105296

Rooney, T. O., Herzberg, C., & Bastow, I. D. (2012). Elevated mantle temperature beneath East Africa. *Geology*, *40*(G32382R1), 27-40. doi: 10.1130/G32382.1

Schaeffer, A., & Lebedev, S. (2013). Global shear speed structure of the upper mantle and transition zone. *Geophys. J. Int.*, *194*(1), 417–449. doi: 10.1093/gji/ggt095

Silver, P. G. (1997). *A Multidisciplinary Experiment across the Kaapvaal Craton.* International Federation of Digital Seismograph Networks. (Seismic Network) doi: 10.7914/SN/XA_1997

Simmons, N. A., Forte, A. M., & Grand, S. P. (2007). Thermochemical structure and dynamics of the African superplume. *Geophys. Res. Lett.*, *34*(2). doi: 10.1029/2006GL028009

Steinberger, B. (2000). Slabs in the lower mantle — results of dynamic modelling compared with tomographic images and the geoid. *Phys. Earth Planet. Int.*, *118*(3-4), 241–257. doi: 10.1016/s0031-9201(99)00172-7

Stern, R. (2004). Subduction initiation: spontaneous and induced. *Earth Planet. Sci. Lett.*, *226*(3), 275–292. doi: 10.1016/j.epsl.2004.08.007

Sun, M., Fu, X., Liu, K. H., & Gao, S. S. (2018). Absence of thermal influence from the African Superswell and cratonic keels on the mantle transition zone beneath southern Africa: Evidence from receiver function imaging. *Earth Planet. Sci. Lett.*, *503*, 108–117. doi: 10.1016/j.epsl.2018.09.012

Sun, M., Liu, K. H., Fu, X., & Gao, S. S. (2017). Receiver Function Imaging of Mantle Transition Zone Discontinuities Beneath the Tanzania Craton and Adjacent Segments of the East African Rift System. *Geophys. Res. Lett.*, *44*(24), 12,116–12,124. doi: 10.1002/2017gl075485

Tauzin, B., Debayle, E., & Wittlinger, G. (2008). The mantle transition zone as seen by global Pds phases: No clear evidence for a thin transition zone beneath hotspots. *J. Geophys. Res.*, *113*(B8). doi: 10.1029/2007jb005364

Thompson, D. A., Hammond, J. O. S., Kendall, J., Stuart, G. W., Helffrich, G. R., Keir, D., . . . Goitom, B. (2015). Hydrous upwelling across the mantle transition zone beneath the Afar Triple Junction. *Geochem. Geophys. Geosyst.*, *16*(3), 834–846. doi: 10.1002/2014gc005648

Tilmann, F., Yuan, X., Rümpker, G., & Rindraharisaona, E. (2012). *SELASOMA Project, Madagascar 2012-2014.* Deutsches GeoForschungsZentrum GFZ. (Seismic Network) doi: 10.14470/MR7567431421

Tosi, N., & Yuen, D. A. (2011). Bent-shaped plumes and horizontal channel flow beneath the 660km discontinuity. *Earth Planet. Sci. Lett.*, *312*(3-4), 348–359. doi: 10.1016/j.epsl.2011.10.015

Utrecht University (UU Netherlands). (1983). *NARS.* International Federation of Digital Seismograph Networks. (Seismic Network) doi: 10.7914/SN/NR

van Stiphout, A. M., Cottaar, S., & Deuss, A. (2019). Receiver function mapping of mantle transition zone discontinuities beneath Alaska using scaled 3-D velocity corrections. *Geophys. J. Int.*, *219*(2), 1432–1446. doi: 10.1093/gji/ggz360

Velasco, A., & Kaip, G. (2011). *Seismic Characterization of Menengai Crater, Kenya.* International Federation of Digital Seismograph Networks. (Seismic Network) doi: 10.7914/SN/1C_2011

Vergne, J., Doubre, C., & Leroy, S. (2014). *Seismic network 7c:dora experiment (resif-sismob).* RESIF - Réseau Sismologique et géodésique Français. (Seismic Network) doi: 10.15778/RESIF.7C2009

Vinnik, L. P., Oreshin, S., Kosarev, G., Kiselev, S., & Makeyeva, L. (2009). Mantle anomalies beneath southern Africa: evidence from seismic S and

P receiver functions. *Geophys. J. Int.*, *179*(1), 279–298. doi: 10.1111/ j.1365-246x.2009.04261.x

Vinnik, L. P., Oreshin, S. I., Speziale, S., & Weber, M. (2010). Mid-mantle layering from SKS receiver functions. *Geophys. Res. Lett.*, *37*(24). doi: 10.1029/ 2010gl045323

Waszek, L., Schmerr, N. C., & Ballmer, M. D. (2018). Global observations of reflectors in the mid-mantle with implications for mantle structure and dynamics. *Nature Communications*, *9*(1), 385. doi: 10.1038/s41467-017-02709-4

Weeraratne, D., Forsyth, D., Fischer, K., & Nyblade, A. (2003). Evidence for an upper mantle plume beneath the Tanzanian craton from Rayleigh wave tomography. *J. Geophys. Res.*, *108*(B9). doi: 10.1029/2002JB002273

Wiens, D. A., & Nyblade, A. A. (2005). *Broadband Seismic Investigation of the Cameroon Volcanic Line.* International Federation of Digital Seismograph Networks. (Seismic Network) doi: 10.7914/SN/XB_2005

Williams, C. D., Li, M., McNamara, A. K., Garnero, E. J., & van Soest, M. C. (2015). Episodic entrainment of deep primordial mantle material into ocean island basalts. *Nature Communications*, *6*(1), 8937. doi: 10.1038/ncomms9937

Williams, C. D., Mukhopadhyay, S., Rudolph, M. L., & Romanowicz, B. (2019). Primitive Helium Is Sourced From Seismically Slow Regions in the Lowermost Mantle. *Geochem. Geophys. Geosyst.*, *20*(8), 4130–4145. doi: 10.1029/2019gc008437

Wysession, M. E., Wiens, D. A., & Nyblade, A. A. (2011). *Investigation of sources of intraplate volcanism using PASSCAL broadband instruments in Madagascar, The Comores, and Mozambique.* International Federation of Digital Seismograph Networks. (Seismic Network) doi: 10.7914/SN/XV_2011

Xu, W., Lithgow-Bertelloni, C., Stixrude, L., & Ritsema, J. (2008). The effect of bulk composition and temperature on mantle seismic structure. *Earth Planet. Sci. Lett.*, *275*(1-2), 70–79. doi: 10.1016/j.epsl.2008.08.012

Ye, Y., Gu, C., Shim, S.-H., Meng, Y., & Prakapenka, V. (2014). The postspinel boundary in pyrolitic compositions determined in the laser-heated diamond anvil cell. *Geophys. Res. Lett.*, *41*(11), 3833–3841. doi: 10.1002/2014gl060060

Yu, Y., Liu, K. H., Moidaki, M., Reed, C. A., & Gao, S. S. (2015). No thermal anomalies in the mantle transition zone beneath an incipient continental rift: evidence from the first receiver function study across the Okavango Rift Zone, Botswana. *Geophys. J. Int.*, *202*(2), 1407–1418. doi: 10.1093/gji/ggv229
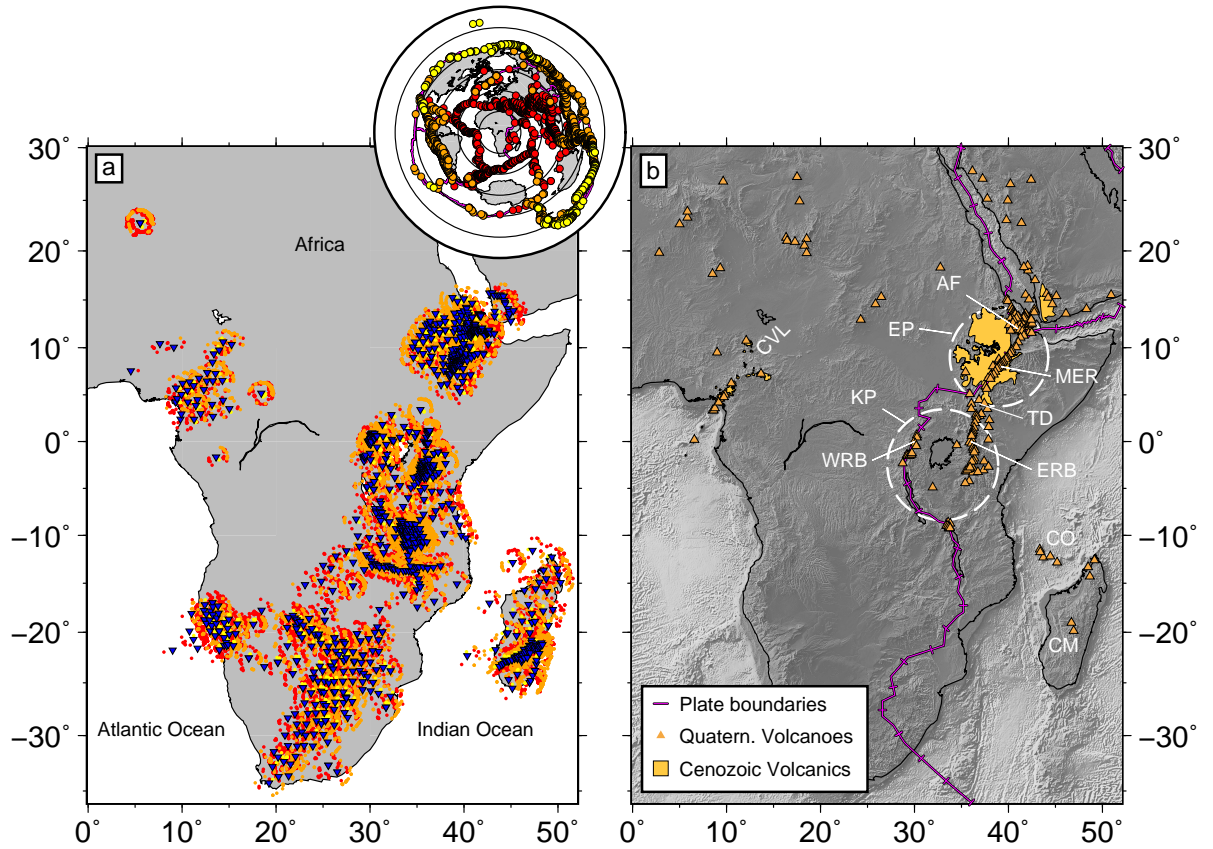
Figure 1. (*a*) Red/orange/yellow circles indicate P410s/PP410s/PKP410s piercing points; 947 seismograph stations are shown as blue triangles. Inset globe shows 2778 unique earthquakes used for three RF data sets using the same colors. (*b*) Quaternary volcanoes and Cenozoic volcanic provinces shown with respect to the main geological features. White dashed circles: the Ethiopian (EP) and Kenyan (KP) topographic plateaus. AF: Afar, CM: Central Madagascan magmatism, CO: Comoros Islands, CVL: Cameroon Volcanic Line, MER: Main Ethiopia Rift, TD: Turkana depression, WRB/ERB: western/eastern rift branches of southern East African Rift System (EAR).
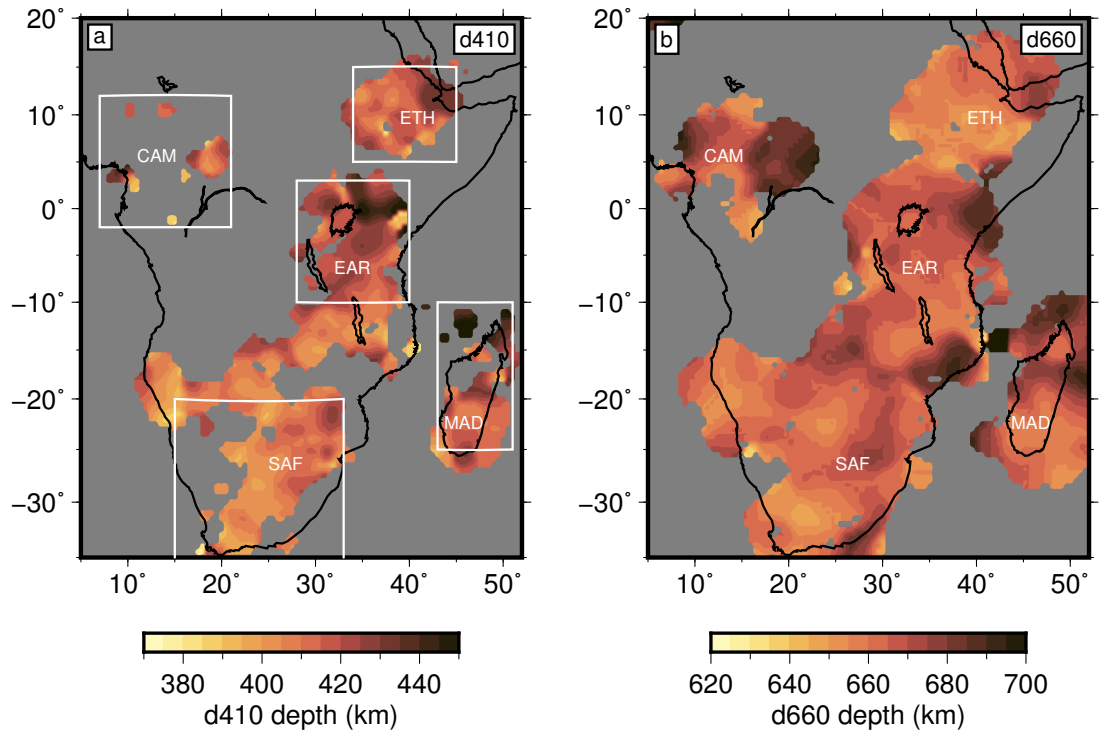
Figure 2. Maps of d410 (*a*) and d660 (*b*) discontinuity depths within AFRP20-CCP using RF data containing maximum frequencies of 0.2 Hz. Regions are shown only where stacking weight is greater than 2 (Figure S6) and relative amplitude is greater than two standard error. Regional discontinuity depths are presented for the five regions outlined in white boxes throughout the manuscript. CAM: Cameroon, ETH: Ethiopia, EAR: East African Rift, SAF: Southern Africa, MAD: Madagascar.
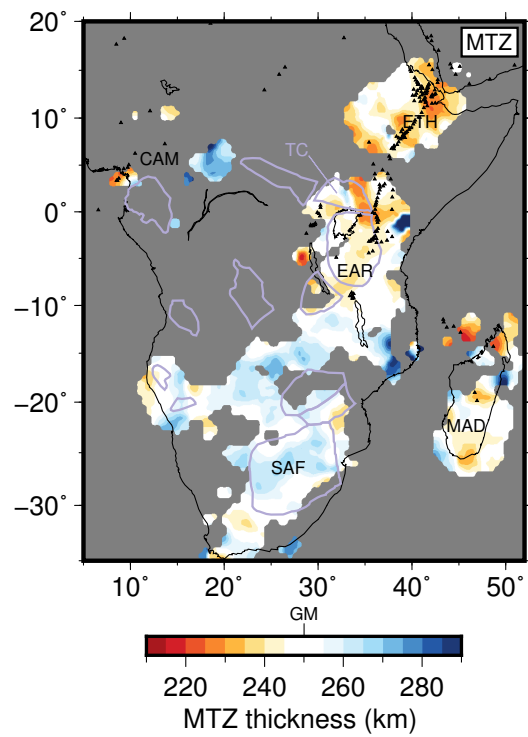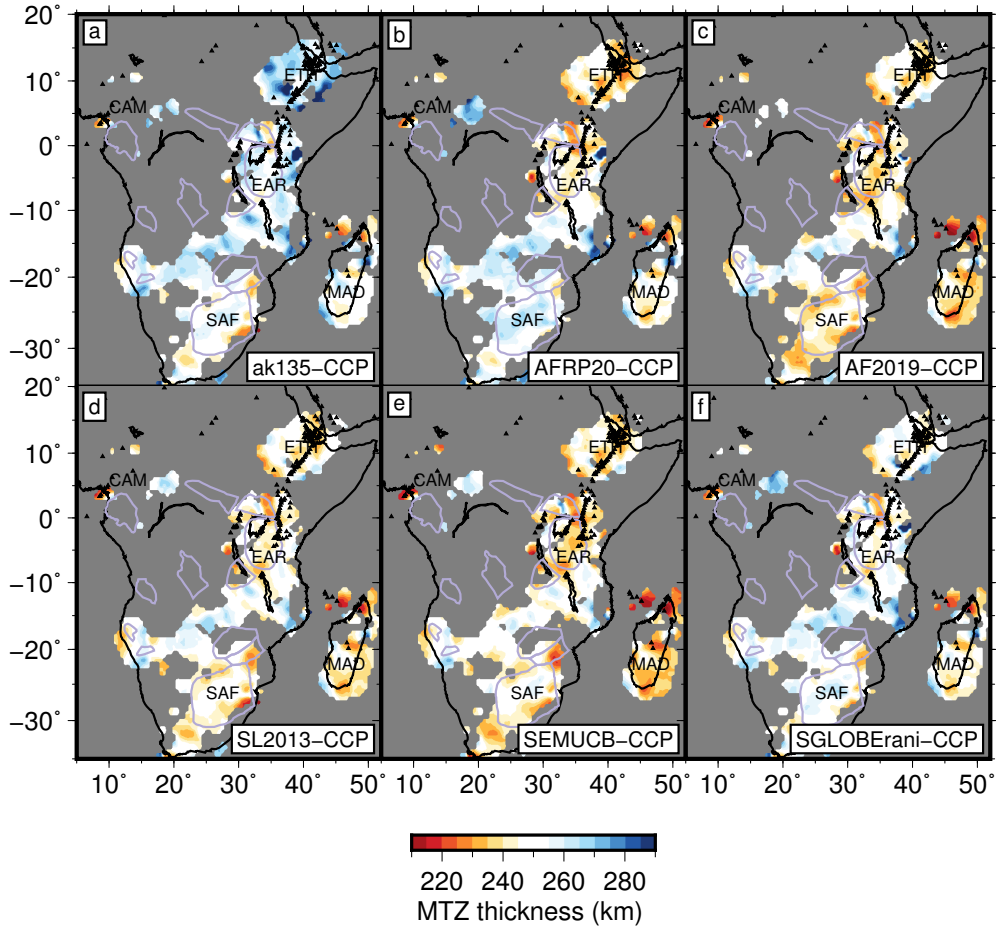
Figure 3. Map of mantle transition zone (MTZ) thickness (d660 – d410) within AFRP20-CCP (Figure 2). Violet lines: outlines of Archean cratons. TC: Tanzanian craton. Black triangles: Quaternary volcanoes. Regions are shown only where both d660 and d410 converted arrivals are significant. Regional acronyms as in Figure 2. GM: Global mean.
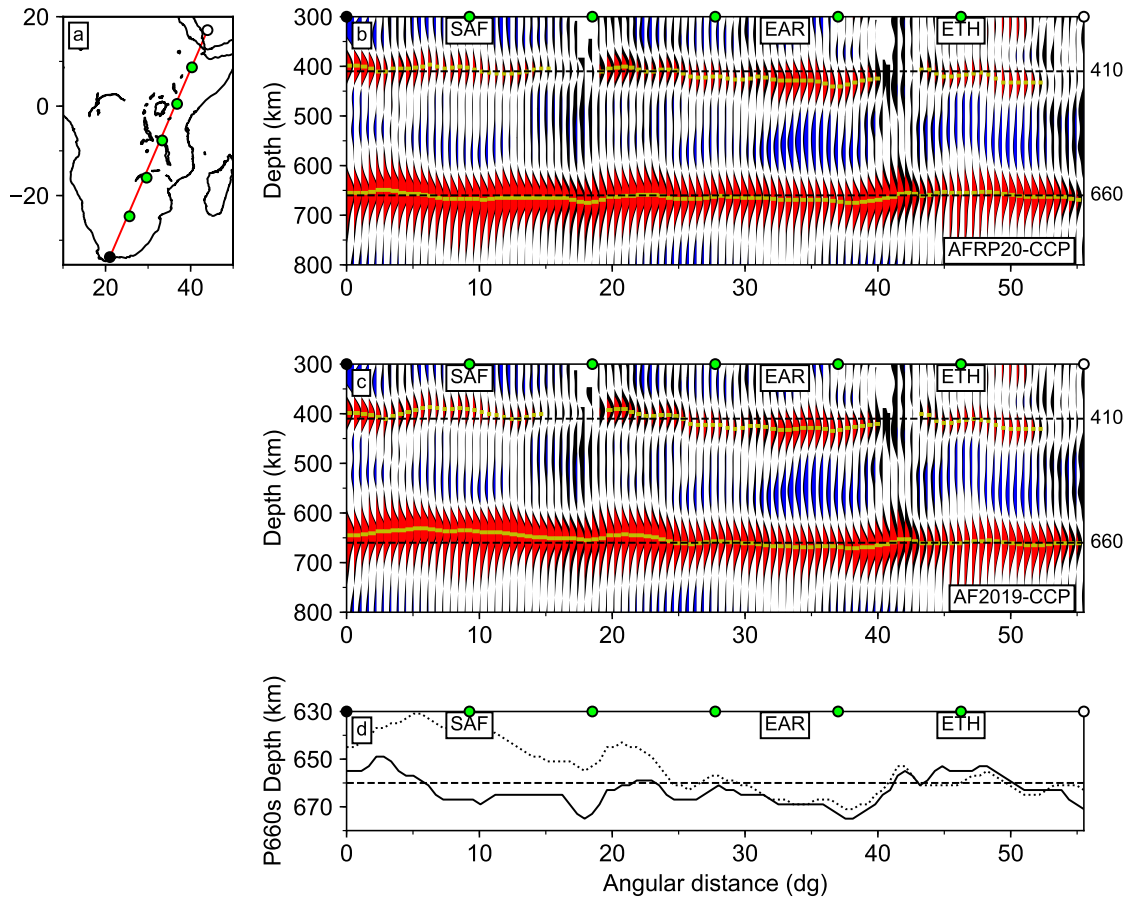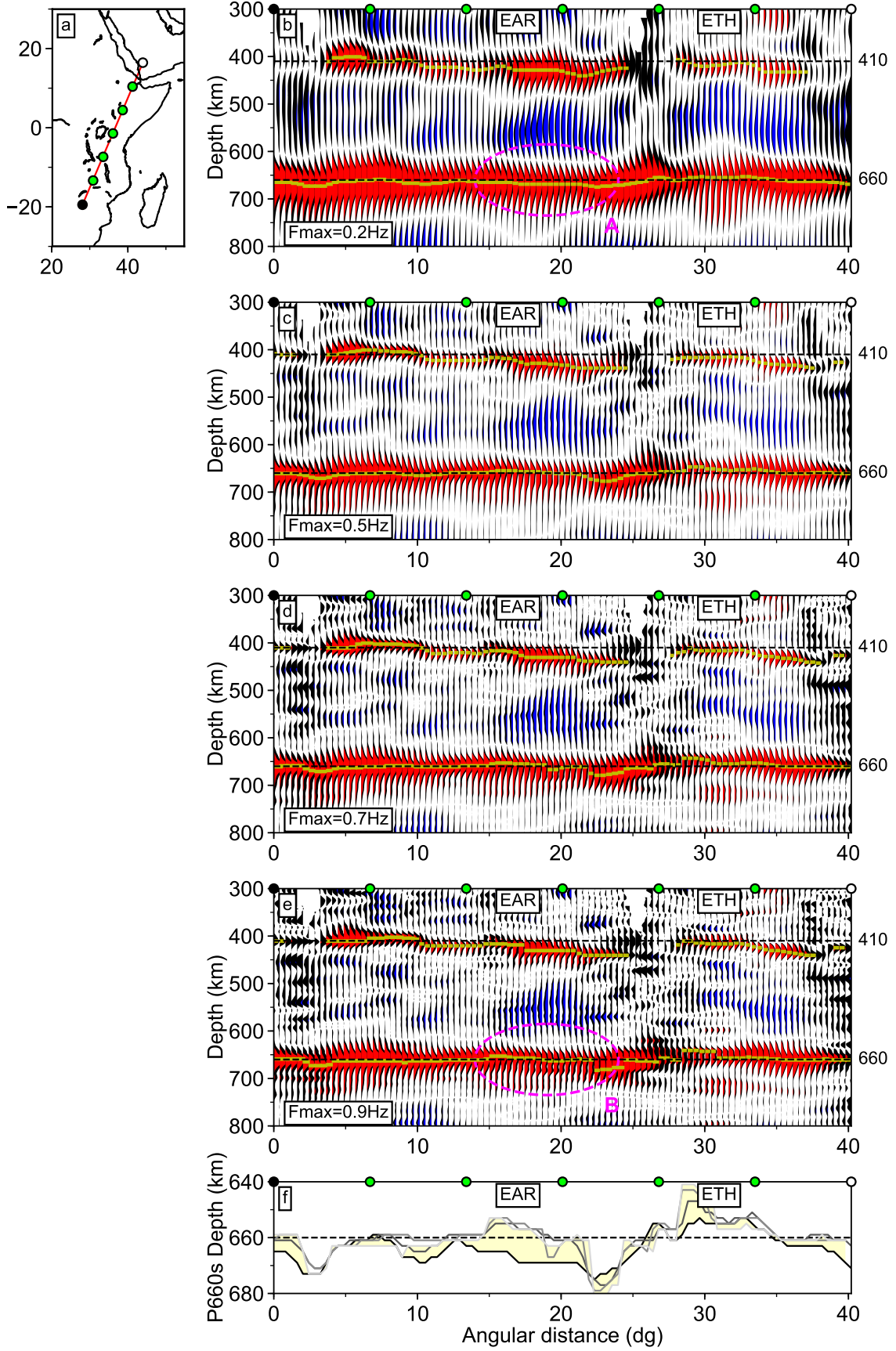
Figure 4. Along the profile (*a*), waveform cross-sections (up to 0.2 Hz) through AFPR20-CCP (*b*) and AF2019-CCP (*c*). Yellow ticks: depths of maximum amplitudes of MTZ discontinuities within regions where peaks are significant. Strong negative peaks in the MTZ often result from coherent stacking of surface multiples. d660 depths within AFRP20-CCP (solid) and AF2019-CCP (dashed) are shown below (*d*). ETH: Ethiopia, EAR: East African Rift, SAF: Southern Africa.

Figure 5. Maps of mantle transition zone (MTZ) thickness (d660 – d410) within ak135-CCP (*a*), AFRP20-CCP (*b*), AF2019-CCP (*c*), SL2013-CCP (*d*), SEMUCB-CCP (*e*), SGLOBErani-CCP (*f*). Regions are shown only where both d660 and d410 converted arrivals are significant. The corresponding plots for d410 and d660 depth as well as the mean and standard deviation d410 and d660 depths derived from the five 3D time-to-depth corrected CCP stacks are included in the Supplementary Material (Figures S9–S12). Violet lines: outlines of Archean cratons. TC: Tanzanian craton. Black triangles: Quaternary volcanoes. CAM: Cameroon, ETH: Ethiopia, EAR: East African Rift, SAF: Southern Africa, MAD: Madagascar.

Figure 6. Along the profile (*a*), waveform cross-sections through AFRP20-CCP of increasing maximum RF frequency from 0.2–0.9 Hz (*b*–*e*). Yellow ticks: depths of maximum amplitudes of MTZ discontinuities where peaks are significant. Magenta ellipses (*A, B*) highlight specific features referred to in the text. d660 depth comparison (*f*) within AFRP20-CCP of increasing maximum frequency (Fmax = 0.2 Hz: black, Fmax 0.5–0.9 Hz: grey lines, dark to light). The yellow region highlights the difference between d660 depth using RF Fmax = 0.2 Hz and 0.9 Hz. ETH: Ethiopia, EAR: East African Rift.
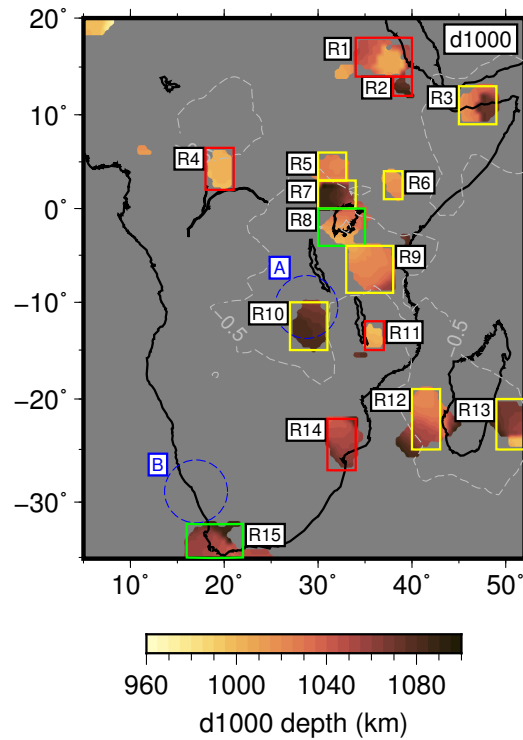

Figure 7. Map of mid-mantle observations in AFRP20-CCP (up to 0.2 Hz). Colored regions highlight depths of significant peaks at mid-mantle depths 960–1100 km. Labeled regions are outlined based on confidence of a true Pds/PPds conversion within the CCP stack based on slowness analysis (see example in Figure 8). High confidence result: green, intermediate: yellow, low: red. Dashed blue regions show location of previous mid-mantle discontinuities observed using using P'P' precursors LeStunff et al. (1995, - A) and using SKSdp phases Vinnik et al. (2010, - B). Grey dashed lines mark the $\delta V_P = -0.5\%$ contour in the AFRP20 tomographic model (Boyce et al., 2021).
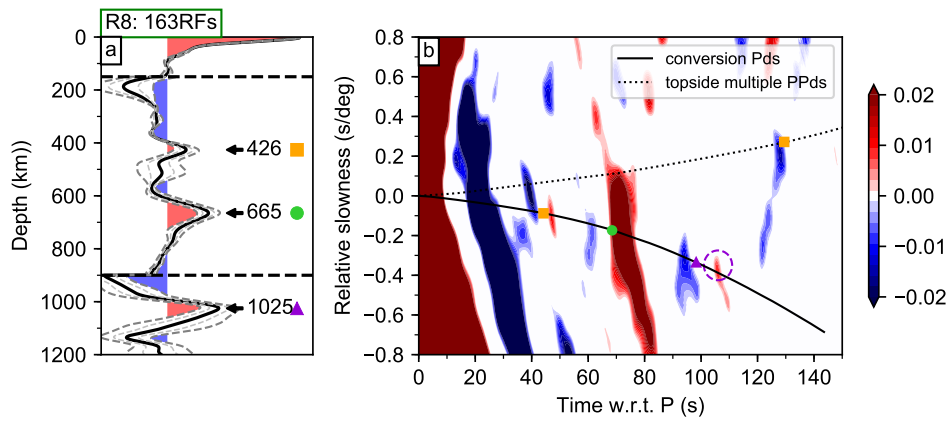
Figure 8. Depth (*a*) and slowness (*b*) stack for 163 Pds RFs whose piercing points at 1000 km depth fall within R8 (see Figure 7). RF max frequency is 0.2 Hz. (a) Depth stack amplitudes are multiplied by five and twenty below 150 km and 900 km respectively. Depth conversion uses the AFRP20 tomographic model (Boyce et al., 2021). The depth of high amplitude positive peaks at and below MTZ depths are labeled. (b) Predicted converted Pds arrivals have negative slowness (solid line), multiples have positive slowness (dashed line) w.r.t. direct-P phase. The number of RFs included in the stack is given in the upper left. A positive high confidence amplitude conversion is observed on the predicted slowness line at ∼106 s (violet dashed circle).
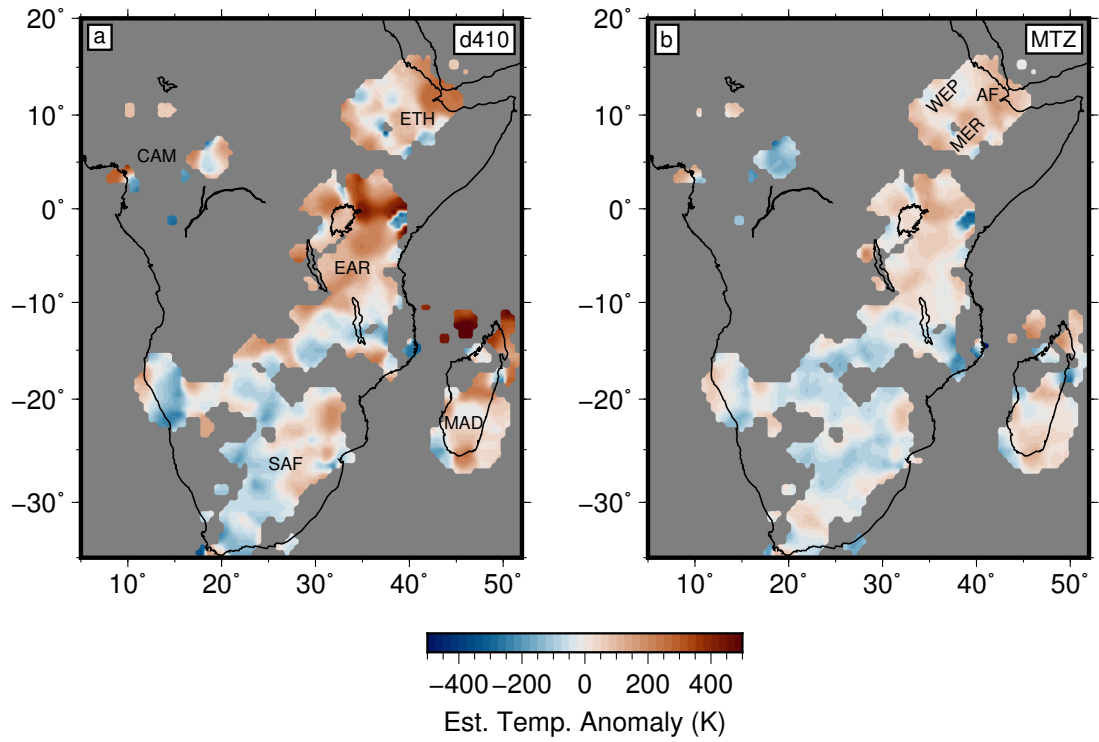
Figure 9. Maps of estimated temperature anomalies within the MTZ derived from AFRP20-CCP (Figures 2, 3). Discontinuity depths are converted to pressure using PREM (Dziewonski & Anderson, 1981). (*a*) Temperature anomaly derived from d410 depths. We assume the temperature anomaly where d410 depth equals 410 km is zero. We assume an average value for the d410 Clapeyron slope of $\delta P/\delta T_{d410}$=3.0 MPa/K (Bina & Helffrich, 1994). (*b*) Temperature anomaly derived from MTZ thickness. We assume the temperature anomaly is zero where MTZ thickness is 250 km. We use the same Clapeyron slope for the d410 as in (*a*) and an average d660 Clapeyron slope of $\delta P/\delta T_{d660}$=−2.5 MPa/K (Ye et al., 2014) for the olivine transition. WEP: Western Ethiopian plateau, other regional acronyms as in Figure 2.
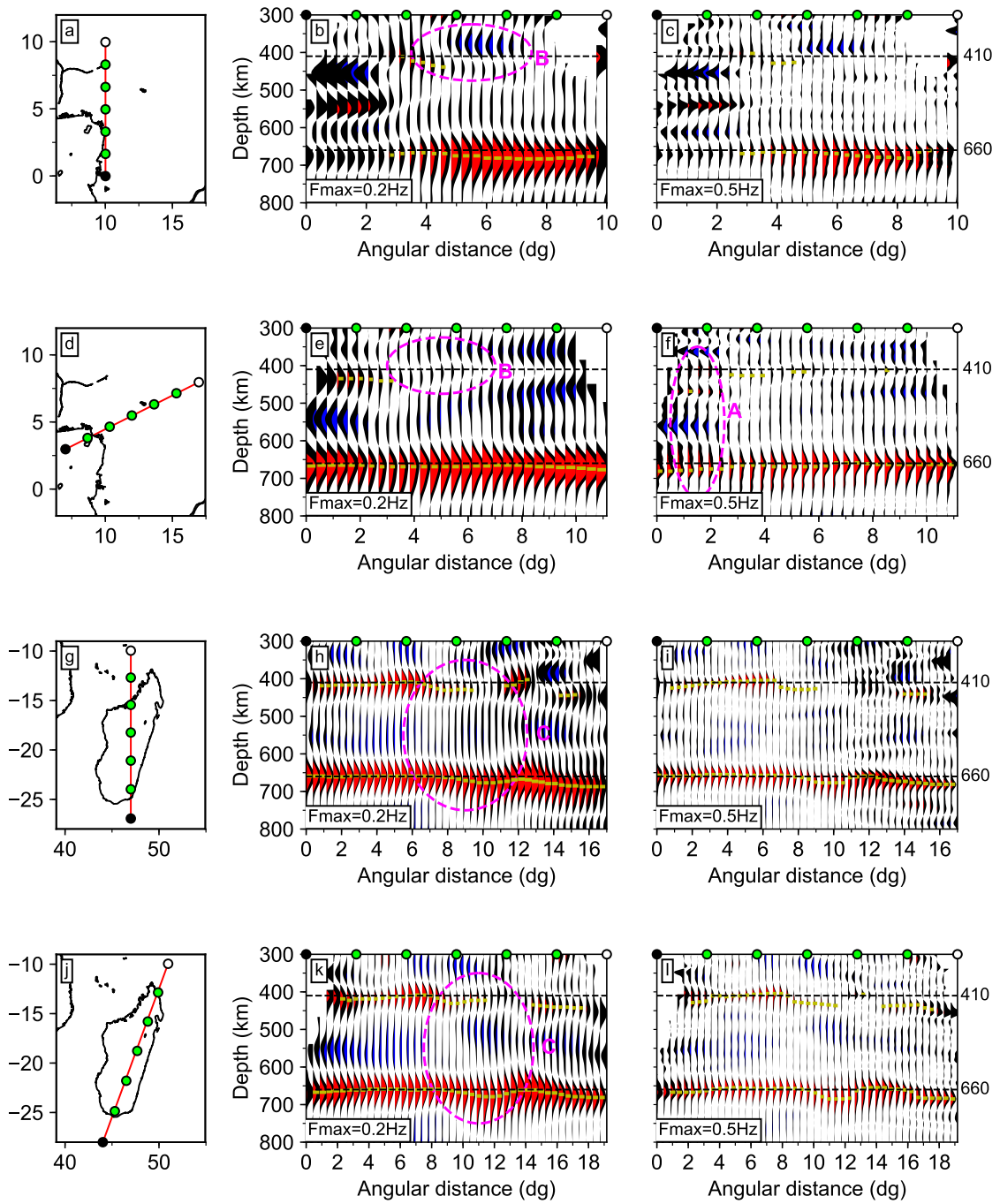
Figure 10. Waveform cross-sections through AFRP20-CCP in Cameroon (a,d) and Madagascar (g,j) using maximum RF frequencies of 0.2 Hz (b,e,h,k) and 0.5 Hz (c,f,i,l). Yellow ticks: depths of maximum amplitudes of significant d660 and d410 converted arrivals. Magenta ellipses (A, B, C) highlight specific features referred to in the text.
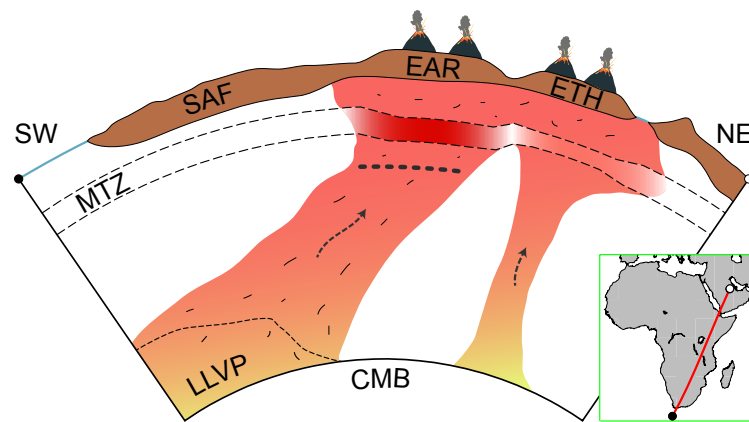
Figure 11. Schematic summary of our favored interpretation along the profile shown in the inset map, including observed high confidence mid-mantle discontinuity topography (thick dashed line), and interpreted anomalous LLVP composition in the southern upwelling below EAR (black flecks). Upwelling below ETH, is likely to be purely thermal in nature and is rooted further east in the lower mantle, but is projected onto the profile for illustration. Topographies on the surface, base of the lithosphere, and mantle discontinuities are exaggerated and not to scale. CMB: core-mantle boundary. Other acronyms follow those in the text.